1	
2	Isolating Spatiotemporally Local Mixed Rossby-gravity Waves
3	Using Multi-dimensional Ensemble Empirical Mode Decomposition
4	
5	
6	Jie Sun and Zhaohua Wu*
7	Department of Earth, Ocean, and Atmospheric Science & Center for Ocean-Atmospheric
8	Prediction Studies, Florida State University, Tallahassee FL 32306, USA
9	August 2019
10	
11	*Corresponding author Email: <u>zwu@fsu.edu</u>
12	
13	Keywords: Mixed Rossby-gravity waves, spectra of tropical waves, spatiotemporal
14	inhomogeneity of tropical waves, Multi-dimensional Ensemble Empirical Mode
15	Decomposition

Abstract

Tropical waves have relatively large amplitudes in and near convective systems, attenuating as they propagate away from the area where they are generated due to the dissipative nature of the atmosphere. Traditionally, nonlocal analysis methods, such as those based on the Fourier transform, are applied to identify tropical waves. However, these methods have the potential to lead to the misidentification of local wavenumbers and spatial locations of local wave activities.

To address this problem, we propose a new method for analyzing tropical waves, with particular focus placed on equatorial mixed Rossby-gravity (MRG) waves. The new tropical analysis method is based on the multi-dimensional ensemble empirical mode decomposition and a novel spectral representation based on spatiotemporally local wavenumber, frequency, and amplitude of waves. We first apply this new method to the analysis of synthetic data to demonstrate the advantages of the method in loyally revealing characteristics of MRG waves. We further apply This new method to reanalysis data (1) to identifyies and isolates the spatiotemporally heterogeneous MRG waves event by event, and (2) to quantifyies the spatial inhomogeneity of these waves in a wavenumber-frequency-energy diagram. In this way, we reveal the climatology of spatiotemporal inhomogeneity of MRG waves and summarize it in wavenumber-frequency domain: The Indian Ocean is dominated by MRG waves in the period range of 8-12 days; the western Pacific Ocean consists of almost equal energy distribution of MRG waves in the period ranges of 3-6 and 8-12 days, respectively; and the eastern tropical Pacific Ocean and the tropical Atlantic Ocean are dominated by MRG waves in the period range of 3-6 days. The zonal wavenumbers mostly fall within the band of 4-15, with Indian Ocean has larger portion of high wavenumber (smaller wavelength components) MRG waves.

Through these results, By expositing the drawbacks of the Fourier transform based spectral analysis widely used in tropical wave climatology analysis, we demonstrate the inability of Fourier spectral analysis to correctly project the energy of local waves onto the wavenumber frequency domain. We then introduce a spatiotemporally local method, the multi-dimensional ensemble empirical mode decomposition, to identify local wave events and further quantify the spatiotemporal inhomogeneity of MRG waves. An analysis of synthetic data using this new approach demonstrates that the characteristics of MRG waves obtained by analyzing individual wave events are highly consistent with those in new marginal wavenumber frequency spectra.

- 46 Finally, we apply this new approach to analyzing reanalysis data of the whole tropical zone,
- 47 demonstrating its effectiveness and revealing the spatiotemporal inhomogeneity of MRG waves.

48

1. Introduction

49

50

51

52

53

54

55

56

57

58

59

60

61

62

63

64

65

66

67

68

69

70

71

Latent heat release associated with the evolution of large-scale convective systems is the primary energy source that drives tropical weather and climate systems. Tropical waves play a significant role in redistributing this energy to non-convective regions and affect the formation and variability of many tropical phenomena, such as the planetary-scale Hadley/Walker circulations (e.g., Lindzen 1974; Hou and Lindzen 1992; Jin and Hoskins 1995) and synoptic-scale hurricanes (e.g., Avila and Pasch 1992; Frank and Roundy 2006; Dunkerton et al. 2008). These tropical waves are also often modulated by spatiotemporally larger-scale climate phenomena, such as El Niño and the Southern Oscillation (ENSO; e.g., Zhang et al. 1997; Kumar et al. 1999), Hadley circulation (e.g., Schneider and Lindzen 1977; Held and Hou 1980; Schneider 2006), quasi-biennial oscillation (e.g., Lindzen and Holton 1968; Baldwin et. al, 2001), and monsoons (e.g., Tao 1987; Webster and Yang 1992; Wang et al. 2005). The nonlinear interactions of tropical waves with other tropical weather/climate systems make it difficult to clearly identify and separate tropical waves, thus calling for more effective methods to quantify them. An important milestone in the study of tropical waves was the formal conceptualization of convectively-coupled equatorial waves (CCEWs; e.g., Wheeler and Kiladis 1999; Wheeler et al. 2000; Yang et al. 2003; Kiladis et al. 2009; Ogrosky and Stechmann 2016). The seminal study of Matsuno (1966), using a shallow-water model, revealed many fundamental features of tropical free waves including wave propagation characteristics, the matching velocity, and geopotential patterns. Many theoretical characteristics of waves revealed by Matsuno (1966) were confirmed by later observations (e.g., Yanai and Maruyama 1966; Wallace and Kousky 1968; Pfister et al. 1993; Tsuda et al. 1994; Wheeler and Kiladis 1999; Haertel and Kiladis 2004). Matusno's work motivated the exploration of the physical origins of various tropical waves and many mechanisms

were proposed, including: wave-CISK (Conditional Instability of the Second Kind; Lindzen 1974;
Chang and Lim 1988; Sui and Lau 1989), thermal origin (Matsuno 1966; Gill 1980; Mapes and
Houze 1995; Wu et al. 2000a, 2000b, 2001; Wu 2003), gross moist stability (Neelin and Held 1987;
Wang and Rui 1990; Emanuel et al. 1994; Raymond 2000; Haertel and Kiladis 2004; Raymond et
al. 2009), and extratropical origin (Kiladis and Weickmann 1992a; Zhang and Webster 1992;
Straub and Kiladis 2003). Indeed, some of these theories helped shape and develop the concept of
CCEWs.

79

80

81

82

83

84

85

86

87

88

89

90

91

92

93

94

Although the conceptualization of CCEWs provides a novel framework for understanding tropical waves, a quantitative definition of CCEWs has not yet been obtained. As expressed directly by the nomenclature of CCEWs, an important physical aspect of CCEWs is the coupling between tropical convective systems and tropical waves. Many observational studies (e.g., Houze and Betts 1981, Graham and Barnett 1987, Kiladis and Weickmann 1992b, Petersen and Rutledge 2001; Matsui et al. 2015) have shown that tropical convective systems are not zonally homogeneous. Strong convective systems typically operate over the maritime continent, the Amazon region, and the tropical African region where surface temperatures are relatively higher compared to other regions of the tropical belt, with the exception of the annually migrating intertropical convergence zone. From a physical perspective, the latent heat released in convective systems excites tropical waves and leads to either the suppression or enhancement of low-level moisture convergence at or near the convective region as the waves propagate away from the excited region. Due to the zonal asymmetry of structures and propagation speeds of different types of waves with respect to the convective region (e.g., eastward Kelvin waves versus westward Rossby waves), the wave-induced, low-level moisture convergence can also be asymmetric in the zonal direction, leading to zonal migration/propagation of the convective systems. The speed of the migration/propagation of the convective system is tied closely to the low-level wave propagation speed (Lindzen 1974; Liu et al. 2019).

Because the atmosphere is dissipative (with a widely accepted dissipation timescale of five to ten days), it is expected that slowly propagating waves such as mixed Rossby-gravity (MRG) waves (with a typical group velocity of 5 ms⁻¹) can only be observed within a few thousand kilometers of the convective systemregion, leading to the formation of preferred wave activity regions. A combination of the observed locality of convective systems, the basic propagation characteristics of tropical waves, and the dissipative nature of a tropical atmosphere implies that tropical waves can be spatially local.

Many traditional tropical wave analyses that use global spatial Fourier transform-based methods in characterizing tropical waves over the whole tropical belt inherit the hidden assumption of the Fourier transform itself—that the wavy structures (Fourier components) extend over the entire spatial domain of data. This hidden assumption contradicts the observed localization of large-scale convective systems; which serve as wave sources, a difference that can potentially lead to misinterpretation of wave characteristics, especially when focusing on the energy of waves of different wavenumbers and frequencies. This point can be demonstrated by inspecting the Fourier spectra of a highly local wave (mathematically represented by a delta-function of a longitude) and a white noise-like signals over the whole tropical belt. A conceptual example of this tendency toward misinterpretation would be Fourier spectrum analysis of a highly local wave (mathematically represented by a delta function of a longitude). The Fourier spectra of both type of signals are flat over the zonal wavenumber domain. which has the same flat spectrum as that of tropical belt spread, spontaneously generated white noise like waves. If only the wave spectrum diagram is inspected, a local wave can easily be misinterpreted as waves occurring over the whole

tropical belt. And when further physical characteristics of tropical waves are inferred from such a wave spectrum, inaccurate interpretations could occur. It is in cases such as this that a method that can identify and separate local waves would be desirable.

In this study, we introduce a newly developed spatiotemporally local analysis method—multidimensional ensemble empirical mode decomposition (MEEMD; Wu et al. 2009)—for tropical
wave analysis. MEEMD has previously been applied to understand climate variability and change
in the case of the evolution of global surface warming (e.g. Ji et al. 2014), the ENSO phenomena
(e.g. Feng et al. 2014), and quasi-biannual oscillation (e.g. Huang et al. 2012). Windowed Fourier
transform and wavelet decomposition have also been used to analyze and capture the local
characteristics of tropical waves (e.g., Meyers et al. 1993; Diedhiou et al. 1999; Whitcher et al.
2000; Chane-Ming et al. 2010; Kikuchi and Wang 2010; Roundy 2012). However, previous studies
have demonstrated that ensemble empirical mode decomposition (EEMD; Wu and Huang 2009),
which is the core of MEEMD, has higher temporal locality than windowed Fourier transform and
wavelet decompositions when they are used to decompose a time series (Wu et al. 2011). In
addition, MEEMD is absolutely spatially local, with the decompositions of time series from
neighboring grid points completely independent. Therefore, it is expected that MEEMD is better
suited to capture the spatiotemporally local characteristics of tropical waves.

This paper is arranged as follows: Section 2 explains the drawbacks of Fourier spectral representation in analyzing tropical waves and introduces MEEMD. Section 3 presents analysis of mixed Rossby-gravity (MRG) waves using MEEMD. It is noted that the MRG waves isolated and analyzed are not exclusively convectively coupled waves in convective region; rather, they may be a mix of convectively coupled waves and free waves. In a non-convective region, they are free

waves. A comparison of our results with previous results is also included. Section 4 details implications of the new tropical wave analysis method in understanding tropical waves.

2. The MEEMD method and the marginal wavenumber-frequency spectrum

The excitation and propagation of the tropical atmosphere approximately follows linear dynamics (Matsuno 1966; Gill 1980; Wu et al. 2000a). An important summary on the characteristics of tropical waves is the dispersion relationship that relates wavenumber, wave frequency, and equivalent depth, with the latter while also characterizing the propagation speed and meridional scale. Thus, an improved determination of wavenumber and wave frequency can lead to improved quantification of meridional scale. As mentioned earlier, the locality of tropical waves in the spatiotemporal domain, partially due to the dissipative nature of the tropical atmosphere, increases the difficulty in accurately determining local wavenumber and wave frequency. The use of MEEMD for tropical wave analysis alleviates this problem.

2.1 Potential misinterpretation of tropical wave characteristics by Fourier spectrum analysis

Fourier transform and Fourier spectral analyses are known as global data domain analysis methods and have been widely applied in tropical wave analysis (Yanai et al. 1968; Maruyama 1969, 1991; Wallace and Chang 1969; Wallace 1971; Takayabu and Nitta 1993; Takayabu 1994a, 1994b; Wheeler and Kiladis 1999; Wheeler et al. 2000; Kiladis et al. 2009) and in the theoretical understanding of tropical waves (Lindzen 1974; Lindzen and Tsay 1975; Straus and Lindzen 2000). While most previous theoretical studies do not distinguish between local and global wavenumber/frequency, the wavenumber/frequency in these studies should be considered local or

tropical belt-averaged since the excited wave cannot survive in the far field and long term due to the dissipative atmosphere. The mismatch between the global domain Fourier transform-based analysis and a theoretically local approach of tropical waves can lead to misinterpretations of tropical wave diagnoses.

To illustrate this point, we look at two synthetic wave fields: one comprised of spatiotemporally homogeneous waves mimicking free waves in a non-dissipative tropical atmosphere and the other spatiotemporally local waves mimicking waves existing only in the neighborhoods of their excitation, taking into account that the atmosphere is dissipative. In the first case, the detailed waveform is given by

171
$$v(x,t) = \frac{1}{3} \sum_{j=1}^{3} \cos(k_j x - \omega_j t),$$
 (1)

- where wave frequency ω_i and wavenumber k_i satisfies the dispersion relationship of MRG waves
- 173 [Eq. (11.42) of Holton (2004)]:

174
$$\omega_{j} = k_{j} \sqrt{g h_{e}} \left[\frac{1}{2} \pm \frac{1}{2} \left(1 + \frac{4\beta}{k_{j}^{2} \sqrt{g h_{e}}} \right)^{\frac{1}{2}} \right], \quad k_{j} \neq 0,$$
 (2)

in which h_e is the equivalent depth and β the meridional derivative of Coriolis parameter at the Equator. Eastward propagating wave (in phase velocity sense) ($k_j > 0$) corresponds to positive root and westward propagating wave corresponds to negative root. An example of wave fields with a specified equivalent depth of 50 m and specified zonal wavenumbers of 8, 12, and 16 (corresponding to wave periods of about 5, 6, and 8 days) is plotted in Fig. 1a. The Fourier spectrum of these synthetic waves captures the correct spectra of the waves, with concentrated

wave energy located at the specified wavenumber and wave frequency pairs corresponding to the specified MRG wave dispersion relationship line, as illustrated in Fig. 1b.

As is already known, MRG waves have small group velocities of a few meters per second. Since convective systems are spatially local and sporadic in temporal domain, spatiotemporally local wave fields are expected. With this in mind, we include the effect of a dissipative atmosphere in constructing our second example of wave fields by adding an amplitude modulation function but without modifying wave carriers, mathematically expressed below:

188
$$v(x,t) = \sum_{j=1}^{3} A_j(x,t)\cos(k_j x - \omega_j t), \qquad (3)$$

where $A_j(x,t)$ is a spatiotemporally slower varying function (compared to the wave period and wave length of the carriers of waves), with their values specified as:

191
$$A_{1} = \begin{cases} \exp\left[-\frac{(x-70)^{2}}{2 \cdot 20^{2}}\right] \left\{ \exp\left[-\frac{(t-67)^{2}}{2 \cdot 9^{2}}\right] + \exp\left[-\frac{(t-175)^{2}}{2 \cdot 5^{2}}\right] \right\}, x \in (0^{\circ}E - 120^{\circ}E), \\ 0, elsewhere \end{cases}$$
 (4a)

192
$$A_{2} = \begin{cases} \exp\left[-\frac{(x-180)^{2}}{2 \cdot 20^{2}}\right] \left\{ \exp\left[-\frac{(t-20)^{2}}{2 \cdot 5^{2}}\right] + \exp\left[-\frac{(t-112)^{2}}{2 \cdot 15^{2}}\right] \right\}, x \in (120^{\circ}E - 60^{\circ}W], \text{ and } (4b) \\ 0, elsewhere \end{cases}$$

193
$$A_{3} = \begin{cases} \exp\left[-\frac{(x-300)^{2}}{2\cdot20^{2}}\right] \left\{ \exp\left[-\frac{(t-67)^{2}}{2\cdot12^{2}}\right] + \exp\left[-\frac{(t-337)^{2}}{2\cdot10^{2}}\right] \right\}, x \in (60^{\circ}W - 360^{\circ}], \\ 0, elsewhere \end{cases}$$
 (4c)

where x is longitude (degree) and t time (day). The second synthetic wave field is comprised of spatiotemporally local waves as displayed in Fig. 1c, of which two wave packets are specified in

each of three individual longitudinal zones. In Eq. 4, the selection of particular parameters that shape the wave field does not change the general spectral characteristics of the wave field as long as the wave field contains spatiotemporal local wave packets.

When two-dimensional Fourier spectral analysis is applied to this wave field, the wave energy is no longer projected mainly onto the correct locations of wavenumber and wave frequency pairs. When the spatiotemporal wave energy distribution is interpreted physically, it implies that these MRG waves are associated with a broad band of equivalent depth based on wave dispersion relationship, which is a misinterpretation of the dynamical features of the original waves.

This drawback of applying Fourier spectral analysis to identifying and separating particular types of tropical waves can be understood using a trigonometric function formula, i.e.,

$$\cos(Kx - \Omega t)\cos(kx - \omega t) = \frac{1}{2}\cos[(k+K)x - (\omega + \Omega)t] + \frac{1}{2}\cos[(k-K)x - (\omega - \Omega)t], \tag{5}$$

where $\cos(Kx-\Omega t)$ is an amplitude modulation function, with K and Ω significantly smaller than k and ω , respectively. Clearly, the right side of Eq. 5 is a Fourier transformation of the left side amplitude modulated wave, with the wavenumber and wave frequency locations of wave energy widely shifted, no longer at the location (k,ω) of wavenumber-frequency domain. Note that this explanation, using $\cos(Kx-\Omega t)$ as an amplitude modulation function, illustrates mathematically the shift and spread of the wave energy band in the wavenumber- frequency domain. If other slowly varying amplitude modulation functions (e.g., a Gaussian function in spatiotemporal domain) are used in Fourier spectrum analysis, a similar shift and spread of wave energy in wavenumber-frequency domain will also be unavoidable, as demonstrated in our second example where we use a Gaussian type of amplitude modulation in spatiotemporal domain. It is noted here

that, as Eq. (5) indicates, this shift and spread of wave frequency is unavoidable regardless of whether a global domain Fourier transform or a windowed Fourier transform is used. Rather, this shift and spread is a general characteristic of using Fourier transform to express amplitude-modulated waves. It is also important to note that the spatiotemporal locality of waves in the atmosphere has already been implied in the seminal paper by Rossby (1939) in which a Cartesian coordinate system and continuous local wavenumber and frequency were used instead of discrete wavenumbers (as in Hough, 1898). The introduction of the concept of group velocity is based on continuously varying (not discrete) wavenumber and wave frequency, which makes it possible to understand wave energy propagation in dynamic meteorology. If a zonally cyclic domain or spherical coordinate is introduced, the completeness and the orthogonality of waveforms (sinusoidal structures on a cyclic domain) or spherical functions would force the waveforms being discrete and hence compromise the concept of group velocity.

2.2 Multi-dimensional ensemble empirical mode decomposition (MEEMD)

The nonlocal characteristics of the Fourier transform in interpreting any time series as the sum of a set of trigonometric functions of constant amplitude and frequency call for improved methods that can identify and separate spatiotemporally local tropical waves. The recently developed MEEMD has been demonstrated to have a high capability for capturing spatiotemporally local signals (e.g., Yan et al. 2011; Rojas et al. 2012; Chang et al. 2013; Li and Misra 2014; Yao et al 2017). The MEEMD method was developed from the EEMD method, which was devised to overcome many drawbacks in the original empirical mode decomposition (EMD) method. EMD represents a new generation of analysis methods for a time series that does not invoke basis functions. This is in contrast to the Fourier transform, which uses trigonometric functions as the basis function, and wavelet analysis, which uses an *a* priori determined mother wavelet as the basis

function. The only assumption associated with EMD is that a component has a wavy form determined adaptively from data and that the amplitude and frequency of the component can vary with time.

2.2a Empirical Mode Decomposition (EMD)

240

241

242

243

244

245

246

247

248

249

250

251

252

253

254

255

256

257

258

259

260

261

The basic idea behind EMD is very simple, as illustrated in Fig. 2. Suppose that a multi-scale time series S(t) (the black curve in Fig.2) is comprised of (1) an amplitude-frequency modulated high frequency wave $a(t)\cos\phi(t)$ and (2) a relatively slowly varying function R(t), where a(t) is a slowly varying non-negative amplitude function and $\phi(t)$ a monotonically increasing function (for defining a non-negative frequency). Clearly, R(t) + a(t) and R(t) - a(t) are the upper and lower envelopes that confine the signal S(t) and R(t) the arithmetic mean of these two envelopes. So, if the upper and lower envelopes of S(t) can be obtained using some method, R(t) can be defined and the difference of S(t) and R(t) is automatically the amplitude-frequency modulated high frequency wave $a(t)\cos\phi(t)$. Two smooth curves, one passing through all the local maxima of S(t) and the other passing through all the local minima, are good approximations to R(t) + a(t) and R(t) - a(t), respectively. The actual algorithm of EMD is directly based on this idea and uses splines fitting through the maxima and minima of a time series S(t) to define upper and lower envelopes. The mean of the two envelopes R(t) is then subtracted from S(t) to obtain the prototype $C_I(t)$. Since spline fitted envelopes can contain errors when they approximate true R(t) + a(t) and R(t) - a(t), the obtained prototype $C_I(t)$ may not be a perfect amplitude-frequency modulated wave that has symmetric upper and lower envelopes with respect to zero mean line. To refine $C_I(t)$, the same process of obtaining R(t) of S(t) is further applied to $C_I(t)$ to obtain $R_I(t)$. $R_I(t)$ is then subtracted from $C_1(t)$ to obtain $C_2(t)$. This process, called "sifting," is repeated as many times as needed until

the upper and lower envelopes of $C_k(t)$ are considered symmetric with zero mean line under some a priori determined criterion, called "stoppage criterion." $C_k(t)$ is designated as the first EMD component $c_1(t)$ of S(t). The difference between $c_1(t)$ and S(t), designated as $r_1(t)$, is subjected to the same sifting process to obtain $c_2(t)$. By subtracting $c_2(t)$ from $r_1(t)$, one obtains $r_2(t)$. The same process is carried out to obtain $c_i(t)$, i=3,4,... until $r_i(t)$ is a trend that is either a monotonic function or contains, at most, one interior extremum over the whole temporal domain (Huang et al. 1998; Wu et al. 2007). In this way, we obtain the decomposition of S(t) as

269
$$S(t) = \sum_{i=1}^{n} c_i(t) + r_n(t) = \sum_{i=1}^{n} a_i(t) \cos \phi_i(t) + r_n(t),$$
 (6)

where $a_j(t)$ and $\omega_j(t) = d\phi_i(t)/dt$ are instantaneous amplitude and frequency of i^{th} component, respectively.

It is noted that, in practice, the sifting number to obtain an EMD component is often fixed to 10, which makes EMD highly local (Wu and Huang 2009) and an almost perfect dyadic filter bank for white noise series (Wu and Huang 2010). It is also noted that the study of waves in the atmosphere and ocean has accompanied the development of the EMD method (Huang et al. 1998; Huang et al. 1999) and its applications (e.g. Zhu et al. 1997; McDonald et al. 2007).

2.2b Ensemble Empirical Mode Decomposition

Since EMD relies on the extrema information to identify and separate riding amplitude-frequency modulated waves, changes in extrema locations and values in data from observation by perturbing the data using intermittent or long-lasting noise may result in significantly different results. For example, if we have two observations of the same physical system that contain minor differences, the EMD decomposition results of these two series are often dramatically different,

which makes accurately inferring physical meaning of individual components almost impossible. In addition, any observational data contain some level of noise and are somewhat a distortion of the true signal. Lack of robustness and the "physical uniqueness" has been a common complaint about the effectiveness of EMD.

283

284

285

286

287

288

289

290

291

292

293

294

295

296

297

298

299

300

301

302

303

304

305

In fact, it is this lack of the robustness of EMD in its decomposition of data that led to the development of EEMD. Wu and Huang (2004) demonstrated that EMD is essentially a dyadic filter bank (with each component having a mean period roughly double its immediately previous component) for white noise. This characteristic of EMD is the starting point for EEMD, which contains the following steps: (1) add a white noise series of a priori determined amplitude, w(t), [often 0.2 standard deviation of that of the targeted data x(t)] to x(t); (2) decompose x(t)+w(t); (3) repeat the previous two steps many times (often more than 100 times), but each time with a different realization of w(t); and (4) take the (ensemble) means of the same ranked components (e.g., c_3) from the decompositions of x(t)+w(t) with different noise realizations as the final result. The rationale for these four steps is as follows: Noise contained in observational data may be nonstationary and even intermittent. In such data, the extrema distribution over the whole temporal domain of data may be quite uneven, leading to an EMD component containing dramatically different timescales. Adding white noise to the original data leads to a relatively even distribution of extrema on all timescales. With this added noise, the decomposition separates scales more effectively. The ensemble approach recovers, to a high degree of accuracy, the original data (the summation of EEMD components) but removes the added noise based on the central limit theorem when the ensemble number is sufficiently large.

The robustness and locality of EEMD decompositions is shown in Fig. 3 where, to demonstrate the robustness of the decomposition, we decompose the meridional velocities of two neighboring

grids (2.5° apart) at the Equator of the NCEP/NCAR (National Centers for Environmental Prediction/National Center for Atmospheric Research) reanalysis for a randomly selected 100-day section. It is visually identifiable that the consistency between corresponding, same ranked modes (e.g., the third mode) is high (Fig. 3a). In addition, systematic differences, such as the systematic leading of the signal at one grid (the top red line) around the 75th day to the corresponding signal at the other grid (the top blue line), are correctly captured in the corresponding modes (the third modes from neighboring grids). In Fig. 3b, we use another approach to demonstrate the locality of EEMD in which the EEMD decomposition is applied to selected data and their shortened versions. It is evident that the decompositions of the overlapped temporal spans are almost identical, especially in high-frequency components, demonstrating that the data at one temporal location only affect the decomposition results of data in very close temporal vicinity. The robustness and the locality of EEMD decomposition suggest that we can indeed identify and isolate local waves of different timescales with a high degree of confidence.

In addition to well-preserved robustness and locality, EEMD also possesses two exciting properties that help deal with the problems of non-stationary and excessive harmonics in data analysis: (1) The temporal locality of an analysis method automatically bypasses the stationarity assumption, which is often applied over the global domain of data; and (2) when EMD/EEMD is applied, the harmonic problem is eliminated. Since EMD/EEMD approximates the envelope of the riding wave using only extrema information, the waveform between two neighboring maxima (minima) is well-preserved; therefore, the harmonics become unnecessary.

2.2c Multidimensional EEMD

One-dimensional data analysis methods (including many time series analysis methods and the EMD/EEMD methods described above) are limited in the capacity to extract spatial-temporally

coherent information contained in multi-dimensional data. MEEMD was developed (Wu et al. 2009) to overcome this limitation. There are two types of MEEMD: one for the decomposition of spatial data such as images, and the other for temporal-spatial data such as gridded climate data, which is the type used in this study. The basic idea behind MEEMD for spatiotemporal data is as follows. Suppose that we have spatiotemporal data X(s,t), where s represents spatial location and t temporal location. Two simple steps are taken to obtain the MEEMD results. First, we decompose the time series, $x_s(t)$, of X(s,t) at spatial location s using EEMD to obtain EEMD components, $c_{i,s}(t)$, for all spatial locations, where the subscript i represents the ith EEMD component of $x_s(t)$. Next, we piece together the i^{th} EEMD component $c_{i,s}(t)$ from all individual spatial locations to form the i^{th} spatiotemporal MEEMD component $C_i(s,t)$. The piecing-together process is also rational: with this improved locality and noise-assisted approach in EEMD, the same ranked components of neighboring grids from EEMD bear similar characteristics, while different ranked components are usually uncorrelated when the neighboring grids data only have small difference (almost always true for climate data). Therefore, the i^{th} components of the s^{th} and the $(s+1)^{th}$ grids are naturally associated. Similarly, the i^{th} components of the $(s+1)^{th}$ and the $(s+2)^{th}$ grids are naturally associated, and so on. This decomposition inherits the temporal locality of EEMD. In a spatial domain, the entire

329

330

331

332

333

334

335

336

337

338

339

340

341

342

343

344

345

346

347

348

349

350

This decomposition inherits the temporal locality of EEMD. In a spatial domain, the entire decomposition process is independent; therefore, MEEMD is absolutely spatially local. The spatiotemporal locality of the method itself guarantees that coherent spatiotemporal structures displayed in MEEMD are not produced by the method; rather, they are characteristic of the data themselves. An example of MEEMD decomposition is presented in Fig. 4, in which the original data is the meridional velocity at 850 hPa level from NCEP/NCAR reanalysis. As discussed earlier,

EEMD is highly temporally local and has low sensitivity to noise. Since the method is based on identifying extrema locations, the signal propagation from one spatial location to its neighboring area (as indicated by the different temporal locations of extrema) can be pinned down. Using this property, we can identify the small variations of different timescales of a climate variable in a neighboring area. Evidently, the third, fourth, and fifth modes $[C_3(s,t), C_4(s,t)]$, and $C_5(s,t)$, respectively] show systematic westward propagations, while the first and second modes $[C_1(s,t)]$ and $C_2(s,t)$, respectively] are more zonally symmetric, either inferring a non-propagating characteristic or a propagation speed that is extremely fast. Note that the averaged periods of the third and fourth modes are about 4.2 days and 8.6 days, respectively, which coincide with many observed MRG wave periods.

Adaptiveness and locality are two of the advantages MEEMD offers. MEEMD does not invoke any significant mathematical constraints such as shape functions (e.g., trigonometric functions in Fourier transform and mother wavelet in wavelet analysis), and its basic ingredient is the "natural" wave form obtained adaptively from data themselves. This inclusion of amplitude and spatiotemporal scale modulations in a component provides the capability of reflecting the complication of the physical world caused by nonlinear interactions and nonstationary external forcing. Additionally, the temporal locality of EMD satisfies a fundamental physical principle: if components extracted from the data reflect the physical processes operating at a given time, then they should be temporally local quantities and the corresponding physical interpretation within specified time intervals should not change with the addition of new data because the subsequent evolution of a physical system cannot alter the reality (which has already occurred). Spatial locality enables MEEMD to identify propagating or expanding signals, and the combination of spatial and

temporal locality in MEEMD offers advantages for examining both standing and propagating waves.

2.3 The marginal wavenumber-frequency spectrum facilitated by MEEMD

373

374

375

376

377

378

379

380

381

382

383

384

385

386

387

388

389

390

391

392

393

394

395

It is also worth looking at whether MEEMD can lead to an improved spectral representation over Fourier-based spectral representation for spatiotemporally local waves. To make this comparison, we first design a local wave-based spectral representation of spatiotemporal data. Because an EEMD component defines an amplitude-frequency modulated signal, we can identify a temporally local frequency and local amplitude at any spatiotemporal location. Similarly, if a local sinusoidal curve fitted to a zonally wavy structure of an MEEMD component is used, we can identify zonal wavenumbers at any spatiotemporal location. In this way, we obtain a set of values, $\{A(s,t), \omega(s,t), k(s,t)\}\$, that are local amplitude, local frequency, and local zonal wavenumber for any spatiotemporal location (s, t). By dividing wavenumber-frequency $(k-\omega)$ space into small twodimensional bins (with a resolution 0.01 cycle per day in frequency and 0.25 in zonal wavenumber) and summing up all of the squares of A(s,t) with their corresponding $\omega(s,t)$ and k(s,t) falling into particular individual two-dimensional bins, we obtain the energy distribution in wavenumberfrequency $(k-\omega)$ space. This approach is an extension of the marginal spectrum for onedimensional data resulting from the Huang transform (Huang et al. 1998) to marginal spectrum representation for two-dimensional $(k-\omega)$ data. For this reason, we refer to our new approach as the marginal wavenumber-frequency spectrum. The detailed description of determining wave amplitude, zonal wavenumber, frequency, and marginal wavenumber-frequency spectrum methods can be found in the Appendix of this paper.

With the marginal wavenumber-frequency spectrum defined, we can now compare the Fourier spectral representation to the marginal wavenumber-frequency spectral representation. Using the

wave field in Fig 5a (which is the same wave field originally shown in Fig. 1c), we illustrate the advantage of the marginal wavenumber-frequency spectral representation. In the marginal wavenumber-frequency spectral representation (Fig. 5b), the wave energy is highly concentrated in three locations consistent with the specified wave frequency, energy, and equivalent depth; dependably catching the characteristics of the synthetic waves specified. In contrast, the Fourier spectral representation (Fig. 1d) of the local wave field has a widely spread energy distribution that can lead to incorrectly inferred zonal wavenumber, wave frequency, and consequently, the equivalent depth. More importantly, the marginal wavenumber-frequency spectrum is highly robust even when the wave field is contaminated by high levels of noise, as the example of noisecontaminated local wave field (Fig. 5c) and its marginal wavenumber-frequency spectrum (Fig. 5d) show. When MEEMD is applied to the noise-contaminated wave field, we obtain a relatively clean wave field by summing the MEEMD components 3 and 4. It is clearly that with a large amount of the noise was removed (Fig. 5e). The corresponding marginal wavenumber-frequency spectrum is now highly concentrated near the specified centers of the wavenumber, frequency, and equivalent depth; again, identifying wave characteristics with high accuracy.

411

412

413

414

415

416

417

418

396

397

398

399

400

401

402

403

404

405

406

407

408

409

410

3. Spatial heterogeneity of mixed Rossby-gravity waves

As discussed earlier, this study seeks to (1) develop tools that will more effectively identify the spatiotemporally heterogeneous tropical waves, and (2) reveal the characteristics of the spatiotemporally heterogeneous tropical waves. The previous section demonstrated that these goals can be achieved using synthetic data. In this section, we apply the MEEMD to analyze observational data and to illustrate the spatiotemporal evolution of various MRG wave events and their projections onto power spectrum diagram in the wavenumber-frequency domain.

The data analyzed in this study are from the NCEP/NCAR reanalysis dataset (Kalnay et al. 1996), which is available at https://www.esrl.noaa.gov/psd/data/gridded/data.ncep.reanalysis.html. The specific data we use are the 850 hPa zonal and meridional winds and geopotential for the temporal range of 1979-2013. The data have a horizontal resolution of 2.5°×2.5° and a temporal resolution of 6-hourly. In the decompositions of these variables using MEEMD, an ensemble number of 1200 and noise magnitude of 0.6 standard deviation of the inputted data subjected to EEMD decomposition at each grid point are selected. The general characteristics revealed are not sensitive to the reanalysis dataset chosen. The analysis of an ERA-interim data (Dee et al, 2011) product from the European Center for Medium-Range Weather Forecasting (ECMWF) leads qualitatively to the same results (not shown).

3.1 The MRG wave events in NCEP/NCAR reanalysis

According to the theoretical framework of tropical waves (Matsuno 1966), wavelengths of the westward propagating MRG waves should be a few thousand kilometers to match reasonable ranges of equivalent depths (from a few meters to a few hundred meters, see Fig.1b), if MRG waves have periods ranging from 3 to 12 days. The existence of these type of waves has been confirmed in a number of observational studies (e.g., Yanai and Maruyama 1966; Liebmann and Hendon 1990; Hendon and Liebmann 1991; Magaña and Yanai 1995; Dickinson and Molinari 2002; Yang et al. 2003; Chen and Huang 2009; Chen and Tam 2012). To discover waves with periods of 3 to 12 days, the third and fourth MEEMD components of zonal winds and meridional winds from NCEP/NCAR 6-hourly reanalysis data that cover this period range are analyzed. We focus more on meridional velocity of waves with a period between 3-12 days because for a realistic equivalent depth range the meridional wind variability, which has the largest amplitude at the

Equator and tailed off meridionally with a Gaussian shape, is mostly associated with MRG waves, as inferred from tropical wave theory (Matsuno 1966).

441

442

443

444

445

446

447

448

449

450

451

452

453

454

455

456

457

458

459

460

461

462

463

The spatiotemporal evolution (Hovmöller diagram) of meridional wind along the Equator at 850 hPa level from the fourth MEEMD component is presented in Fig. 6, where only grid points with wind values larger than 1 ms⁻¹ are displayed. Note that the threshold 1ms⁻¹ is subjectively selected only for the purpose of providing a clearer display of wave pattern. A gross inspection leads to the conclusion that the zonal scales of individual wave events span between about 15° and 50° in longitude, and the periods vary between about 7 to 10 days, which is largely consistent with anticipated theoretically derived MRG waves' dispersion relationship (e.g., Matsuno 1966; Cane and Sarachik 1976; Kiladis et al 2009; and Fig.1b of this paper). Evidently, these wave events are distributed heterogeneously over the spatiotemporal domain with similar periods but quite different zonal wavelengths over the equatorial cycle. Individual wave propagation events can be identified; among them, a large majority have westward (negative) phase velocity. It can also be seen that waves over the western Pacific Ocean region are modulated by intra-seasonal timescale oscillations. This inhomogeneity of the wave signals confirms the necessity advantage of using the MEEMD method rather than more traditional methods, according to the synthetic data experiments demonstrated in Figs. 1c-1d and Fig. 5.

One visually identifiable feature of the wave events displayed in Fig. 6 is that the large wave activities are separated into four equatorial regions: the Indian Ocean, the western tropical Pacific Ocean, the eastern tropical Pacific Ocean, and the equatorial Atlantic Ocean, where convective activity prevails. For convenience in further quantifying MRG wave characteristics, the global tropical belt is divided into four zonal regions, with the names of regions corresponding to the four strong wave activity regions above: the Indian Ocean (20°E–120°E), the western tropical Pacific

(120°E–140°W), the eastern tropical Pacific (140°W–40°W), and the equatorial Atlantic (40°W–20°E).

464

465

466

467

468

469

470

471

472

473

474

475

476

477

478

479

480

481

482

483

484

485

486

To further confirm the characteristics of these wave activities, individual wave events are examined. Fig. 7 illustrates the meridional velocity evolution of one particular wave event based on the fourth MEEMD component in the western tropical Pacific from 8 October to 12 October of 2002. In this figure, the original meridional wind (the central column in Fig. 7b), the MEEMD component 4 (the left column in Fig. 7a), and the Fourier-based filtering result (period range 6-12 days, zonal wavenumber range 6-18, the right column in Fig. 7c) are displayed side by side. A positive meridional wind band (to the west of the 170°E meridional line) and a negative meridional wind band (to the east of the 170°E meridional line) across the Equator is visible on 8 October in the original meridional wind field (Fig. 7b) and in its MEEMD component 4 (Fig. 7a). On the subsequent days, these bands slowly propagate westward, showing a westward phase velocity. In the meantime, the amplitude of the western positive meridional wind band reduces as time goes on, while the amplitude of the original eastern negative meridional wind band is enhanced. To the east of the original negative meridional wind band centered at about 172°E on 8 October, a new crossing-equator positive meridional wind band develops. Although the group velocity cannot be accurately determined without careful calculation of wave amplitude, these features illustrate the eastward wave energy propagation. The evolution with an ~5 ms⁻¹ westward phase velocity and an apparent eastward group velocity, about 1 ms⁻¹, of crossing-equatorial wind bands implies that MRG waves are the main components of the extracted wave activities in this wave event, see Fig. A1 in the Appendix. Note that the fourth MEEMD component captures well the ridge or trough locations that appeared in the original meridional wind field at the Equator. In contrast, the Fourierbased result identifies two additional ridges or troughs, one each to the east and west sides of the

visually identifiable wave activity in the original meridional wind field. The above contrasting results imply that MEEMD does indeed have high locality.

To further confirm that the wave event at the equatorial region contains a large number of MRG waves, we decompose the zonal wind and geopotential using MEEMD and combine the fourth components of the corresponding horizontal wind and geopotential to obtain the full wave field and its evolution. These full wave fields are compared to that of a theoretical MRG wave field of non-dissipative atmosphere, as illustrated in Fig. 8. Focusing on the equatorial region, we see that the extracted full wave fields (including horizontal wind and geopotential) are structurally similar to that of the theoretical solution, although the extracted daily wave field has amplitude modulation while the theoretical solution does not. This is consistent with the earlier discussion of slowly propagating waves in a dissipative atmosphere. Note that there are strong wave fields in the upper left-central portion (off equatorial region) for all days that appear to resemble the tropical depression type of waves (Takayabu and Nitta 1993, Kiladis et al. 2009).

Fig. 6 shows that wave activities extracted from meridional winds at 850 hPa velocities have high spatiotemporal inhomogeneity, possibly consisting of different zonal wavenumbers and wave frequencies. Fig. 9 displays typical wave activities based on meridional winds for the other three regions. In general, the fourth mode of meridional winds in these three regions has similar characteristics to those of the western tropical Pacific: (1) zonally alternating crossing-equatorial wind bands, (2) clear westward phase propagation, and (3) eastward group velocity and energy propagation. Although Fig. 9 only shows the meridional wind field for comparison with the above three criteria, the corresponding horizontal wind field at the 850 hPa level and the geopotential field again confirm that these events have dominant components of MRG waves in the equatorial latitudes (figure not shown). Noticeable differences in the characteristics of these wave events in

different regions are their zonal and meridional scales. For example, the wave event in the Indian Ocean region (see panels a-e of Fig. 9) has a smaller meridional scale, a smaller zonal scale, smaller amplitude, and a smaller phase speed. These differences motivate us to quantitatively examine all individual wave events in different spatiotemporal ranges and to characterize the MRG waves (e.g., typical zonal wavelengths and frequencies).

3.2 The MRG wave climatology in NCEP/NCAR reanalysis

To study the climate of MRG waves, we analyze NCEP/NCAR reanalysis for the period 1979-2013. The climatology is displayed in the form of energy projection onto zonal wavenumber-frequency domain, similar to a Wheeler-Kiladis diagram, but with zonal wavenumber and frequency determined spatiotemporally locally, as outlined in section 2.3. The results for year 2002 and for the whole 35-year span are displayed in Figs. 10a and 10b, respectively. The red noise background-normalized power spectrum of 850 hPa-level meridional wind obtained using the Fourier-based method can be found in Figure 10b of Gehne and Kleeman (2012). It is noted here that the Wheeler-Kiladis diagram shown in Fig. 10b of Gehne and Kleeman (2012) displays the relative strength of the power spectrum with respect to a highly smoothed background red noise spectrum while ours display the power spectrum of local individual MRG wave events without normalization. Therefore, a direct comparison between our marginal spectrum and the normalized spectrum of Wheeler-Kiladis type may not be a well-justified choice.

The one-year <u>elimatology spectrum</u> and the 35-year <u>spectral</u> climatology of MRG waves largely agree when they are displayed in a Wheeler-Kiladis diagram, implying that a one-year <u>elimatology spectrum</u> of relatively frequently occurring MRG waves may represent well the long-

term climatology, at least from the perspective of energy projection onto a zonal wavenumberfrequency domain. Our results show that the observed MRG waves project their energy mostly onto two bands. The first band has a zonal wavenumber range of approximately 4–12 and a period range of 4–6 days with maximum energy located near zonal wavenumber 5 and a 5-day period. The portion of the band with zonal wavenumbers smaller than five largely falls within the wavenumber-frequency domain of equivalent depth ranging from 25 m (corresponding to a gravity wave speed or Kelvin wave speed of about 16 ms⁻¹) to a few thousand meters (corresponding to a gravity wave speed or Kelvin wave speed being close to sound wave speed). Part of the other portion of the band with zonal wavenumbers greater than eight cannot find a corresponding equivalent depth because the identified wavenumber-frequency pair falls outside of the range limited by an infinitely large equivalent depth. Currently, we do not have a theoretical explanation for that portion of the band, although we suspect that the Matsuno's solutions to the shallow water equation linearized with respect to zero mean may not be applicable to this case. As showed in Yang et al. (2003), including the effect of non-zero zonal mean flow can modify the dispersion relationship. The second band has zonal wavenumbers ranging from 5–12 and a period range of 8–10 days with maximum energy located near zonal wavenumber 8 and a 9-day period. This band appears to match equivalent depths on an order of meters. We suspect that this band is associated with waves excited by shallow convective heating. However, more work needs to be done to confirm this explanation.

532

533

534

535

536

537

538

539

540

541

542

543

544

545

546

547

548

549

550

551

552

553

554

Both one-year climatology and long-term climatology of MRG differ significantly from the corresponding results analyzed using red noise-normalized, global-domain Fourier spectral representation, e.g., Fig. 10b of Gehne and Kleeman (2012). As mentioned earlier, a direct comparison between the marginal spectrum and the Wheeler and Kiladis' red noise-normalized

spectrum may not be appropriate. However, our results are consistent with those obtained using spatiotemporally local analysis from other studies, e.g., Fig. 8 of Liebmann and Hendon (1990). While this difference may be attributed significantly to the change from a global view of zonal wavenumber and frequency to a local view, it may also partly be caused by capturing waves from different variables: In Wheeler and Kiladis (1999), the waves were analyzed from outgoing longwave radiation (OLR), while in Liebmann and Hendon (1990) and this study, they are analyzed from 850 hPa-level winds. The reason for this is that OLR is not a dynamical variable directly incorporated in the governing equations from which the wave dispersion relationship is derived (Matsuno 1966), while OLR more represents the heating to excite waves and is tied elosely to slowly varying spatially inhomogeneous sea surface temperature.

In Fig. 11, energy projections onto zonal wavenumber and frequency domain for different longitudinal zones in the tropics confirm that MRG waves have spatially different characteristics. Over the equatorial Indian Ocean, MRG waves tend to have more energy associated with slower propagating waves corresponding to small equivalent depths. Over the equatorial western Pacific and maritime continents region, the two-bands structures mentioned previously are most evident. Over both the equatorial eastern Pacific and the equatorial Atlantic Ocean, the MRG wave energy at a high frequency band is larger than at a low frequency. This higher frequency band contains, at least partly, the effect of Doppler shift caused by predominately easterlies over equatorial Eastern Pacific and equatorial Atlantic Oceans. However, to determine this effect requires the accurate identification of the spatiotemporally varying mean flow on which the MRG waves are riding on, a task we are still making effort to accomplish. In general, there is more MRG wave energy over Indian Ocean and western Pacific regions than over the eastern Pacific and Atlantic Ocean regions. These results appear to be consistent with our hypothesis that MRG waves have a

significant portion being excited and modulated by intraseasonal oscillations (also see Fig. 6) in which shallow convection plays a major role (e.g., Wu et al. 2003): the synoptic timescale MRG waves appear to be intensified in major intraseasonal oscillation events, consistent with the convective heating released in more active westward propagating mesoscale convective clusters on synoptic timescale in intraseasonal oscillation events which have the largest amplitude over Indian Ocean and western Pacific regions.

584

585

586

587

588

589

590

591

592

593

594

595

596

597

598

599

600

578

579

580

581

582

583

4. Summary and Discussions

Over the past few decades, substantial progress has been made in understanding the origins of tropical waves and their interactions with many climate phenomena. This progress has been facilitated by continuous improvements in the observation of tropical weather/climate systems, as well as methods for diagnosis. Historically, the diagnosis of tropical waves has been accomplished in one of two ways: (1) through case studies of tropical waves that revealed highly spatiotemporally local characteristics of tropical waves (e.g., Liebmann and Hendon 1990; Takayabu and Nitta 1993; Dunkerton and Baldwin 1995; Dickinson and Molinari 2002; Nakamura et al. 2003); and (2) using tropical wave climatology to characterize the averaged features of tropical waves over a global spatial or/and temporal domain (e.g., Wheeler and Kiladis 1999; Wheeler et al. 2000; Kiladis et al. 2009; Dias and Kiladis 2014, 2016; Kiladis et al. 2016). However, some characteristics revealed using these two different approaches do not match. For example, the observed MRG waves from a case study were mostly on wavelengths of a few thousand kilometers (e.g., Liebmann and Hendon 1990; Takayabu and Nitta 1993; Dunkerton and Baldwin 1995; Dickinson and Molinari 2002) while the tropical wave climatology revealed that MRG waves can have larger energy projections on planetary scales (e.g., Wheeler and Kiladis 1999; Wheeler et al.

2000; Kiladis et al. 2009). Reconciling these differences and bridging these two approaches remains a challenge.

In this study, we propose a new tropical wave analysis approach and demonstrate its applicability to identify and isolate the spatiotemporally heterogeneous MRG waves. The spatial heterogeneity of MRG waves is summarized using Wheeler-Kiladis-type diagrams. After demonstrating some deficiencies of the Fourier transform-based spectral analysis approach to project energy onto the correct wavenumber-frequency domain for spatiotemporally local waves, we recommend the use of a spatiotemporally local method in MEEMD to characterize local wave events and climatological tropical waves. Our analysis of synthetic data using this new approach demonstrates that the characteristics of tropical waves obtained by analyzing individual wave events are highly consistent with those in the new marginal wavenumber-frequency spectra. We then apply this new approach to real-world reanalysis data and demonstrate its effectiveness. Finally, we show that MEEMD can pick up the spatiotemporal inhomogeneity of MRG waves based on a reanalysis dataset for the entire tropical zone.

Another major difference of our marginal power spectrum in wavenumber-frequency domain from the Wheeler-Kiladis diagram is that the amplitude used for calculating spectral power, wavenumber, and frequency are spatiotemporally locally derived from the identified individual MRG wave events. Although the identified MRG waves guided by various characteristics of theoretical MRG waves are not free of error, our approach bypasses the identification of background noise in traditional Fourier-based MRG wave analyses, such as in Wheeler and Kiladis (1999).

In this study, we do not identify the eastward propagating MRG waves because we searched MRG wave events only in MEEMD modes three and four. The eastward propagating MRG waves, in general, have higher frequencies (smaller periods) than the westward propagating MRG waves. The eastward propagating MRG wave events are likely hidden in MEEMD mode two in the 6-hourly reanalysis data. It remains to be validated whether a similar MRG wave identification method guided by theoretical MRG wave characteristics can help us identify eastward propagating MRG waves.

A hidden philosophical change in our proposed new approach as compared to global data domain Fourier transform-based approaches is the emphasis on tropical waves being forced waves in a dissipative atmosphere rather than the assumption of them as free waves in an inviscid atmosphere. The former approach takes the observed reality that tropical waves are amplitude-frequency modulated while the latter assumes the spatiotemporal homogeneity. It is also important to note that the adaptive nature and spatiotemporal locality of the MEEMD method does not forbid large-scale coherence. If data contain large spatiotemporal coherences, the MEEMD method has the ability to identify these coherences.

The goal of our study and subsequent work is to characterize tropical waves and improve the understanding of tropical waves. Over the past two decades, we have witnessed a philosophical change in our understanding of tropical waves from free waves to convectively coupled waves. New evidence has been revealed that confirms the importance of different types of convection in exciting tropical waves with varying characteristics, such as propagation speed, wavenumber, wave frequency, wave energy distributions, and upper-lower level contrasts. Due to space limitations, these will be reported in detail in future manuscripts.

644	
645	5. Acknowledgement
646	This study has been supported by the National Science Foundation grants AGS-1139479 and
647	AGS-1723300.
648	

Appendix: Algorithm for Obtaining Marginal Spectrum of Mixed Rossby-Gravity Waves

The detailed algorithm includes four major steps: (1) use MEEMD to decompose horizontal winds onto spatiotemporally coherent wave fields; (2) use theoretical MRG wave properties to identify MRG wave events; (3) determine spatiotemporally varying wavenumber, frequency, and amplitude of MRG waves using a local sinusoidal fitting method; and (4) synthesize the MRG wave characteristics by projecting MRG wave energy onto a wavenumber-frequency domain to obtain the marginal spectra of different regions. Steps 1 and 4 are introduced in section 2 of the main manuscript. In this appendix, we introduce technical details of steps 2 and 3.

a. Identifying MRG wave events

As mentioned in section 2, the identification of an MRG wave event uses three-four properties of theoretical MRG waves derived by Matsuno (1966): (1) the westward propagating MRG waves have periods ranging from 3 to 12 days if the corresponding wavenumbers are no larger than 20; (2) the horizontal wind fields are equatorially trapped and should resemble the theoretical structure illustrated in Fig. 8a; (3) the westward propagating MRG waves should have a westward phase velocity; and (4) the westward propagating MRG waves should have a eastward group velocity. In this study, all four steps are used for the identified MRG events for the year 2002.

The first criterion leads to us to only screen the MEEMD components 3 and 4 because only these two MEEMD components have periods falling within the theoretically derived period range. The second criterion is the most important for the screening stage; only the wave events hidden in the MEEMD third and fourth components exhibiting alternating meridional wind in the zonal direction with a one-half wavelength larger than 800 km and an amplitude structure close to a

Gaussian-distribution in the meridional direction (criterion 2) are considered as potential MRG wave events.

670

671

672

673

674

675

676

677

678

679

680

681

682

683

684

685

686

687

688

689

690

The usage of criterion 3 and 4 is illustrated in Fig. A1, in which the meridional wind at the Equator from the fourth component illustrated in Fig. 7a are plotted. The wind at the e-quator from the fourth component is not very smooth, leading to difficulty in identifying the exact spatial location of a ridge (or trough). To overcome this problem, the fourth component of the meridional wind at the equator (spatial series, lines in Fig. A1a), for any given temporal location, is further decomposed using EEMD. The second component of this new decomposition captures the dominant oscillatory patterns. By tracking the sequential longitudinal locations of a ridge, as illustrated by the bold blue dashed arrow (Fig. A1b), the phase speed is determined. Similarly, by tracking the sequential longitudinal location change of a ridge of the envelope (red curves in Fig. Alb), the group velocity is determined. If a sequential event has a negative phase speed and a positive group velocity, we identify the event as an MRG wave event. Since group velocity of MRG waves is usually small, a minor error may lead to a sign change. In practice, we change the positive group velocity criterion to group velocity greater than -0.5 ms⁻¹ to tolerate any potential calculation error. The selection of -0.5 ms⁻¹ is arbitrary, but our sensitivity tests showed that the sensitivity of the results in this study is not sensitive to this particular small negative value since large negative group velocity cases rarely occurred in MEEMD components 3 and 4 rarely occurred.

b. Determining amplitude, local wavenumber, and frequency

According to Matsuno (1966), the meridional wind of MRG wave has the form

691
$$v = A \exp\left(-\frac{y^2}{L^2}\right) \cos(kx - \omega t + \phi), \tag{A1}$$

where A is amplitude, y distance from the equator, L the meridional scale, k local zonal wavenumber, and ω local frequency. A completely rational fit to obtain the amplitude requires a three-dimensional surface membrane fit in space of x, y, and t, which presents both technological and computational difficulties. To avoid this obstacle, for any spatiotemporal location at the Equator (x, 0, t), we use three one-dimensional fits: (1) fitting v(y) from a MEEMD component at any temporal and zonal location with a Gaussian curve to obtain A_y ; (2) fitting v(t) from a MEEMD component at any temporal and zonal location with a sinusoidal function to obtain A_t and local frequency ω ; and (3) fitting v(x) from a MEEMD component at any temporal and zonal location with a sinusoidal function to obtain A_x and local wavenumber k. The reason we use three different amplitude fitting methods is that for a given temporal at the Equator, there is always a possibility that waves are not at the ridge or the trough phase in either the temporal or equatorial zonal domain. Theoretically, the maxima among (A_y, A_x, A_t) should be the true amplitude if the fitting domain in each direction covers a sufficiently large domain. The fitting amplitude corresponding to Fig. 6 is presented in Fig. A2.

In this study, the meridional grid of data for fitting A_y is from 10°S to 10°N. In sinusoidal fitting for A_t in the temporal domain, the window size is 7 days for MEEMD component 3 and 20 days for MEEMD component 4. In sinusoidal fitting for A_x in the zonal domain, the window size is 50° in longitude for component 3 and 30° for component 4. All of these fits use the MATLAB fit function. The window sizes are selected as a balance between locality and accuracy. For the purpose of locality, the window size should be as small as possible. For a sinusoidal fitting to have sufficient accuracy, a piece of data containing a positive maximum and negative minimum is a necessary condition; otherwise, the data themselves do not satisfy the minimum form of an oscillatory pattern. Exhaustive tests show the fitted amplitude, frequency, and wavenumber are not

sensitive to the minor changes of window sizes, such as meridional window change from 10°S to 10°N to 15°S to 15°N, temporal window in the range of 5-10 days for MEEMD component 3 and 10-25 days for MEEMD component 4, and zonal window size varying by 20%.

719 REFERENCES

- Avila LA and Pasch RJ (1992) Atlantic tropical systems of 1991. Monthly Weather Review 120:
- 721 2688-2696. https://doi.org/10.1175/1520-0493(1992)120<2688:ATSO>2.0.CO;2.
- Baldwin MP, Gray LJ, Dunkerton TJ, Hamilton K, Haynes PH, Randel WJ, Holton JR, Alexander
- MJ, Hirota I, Horinouchi T and Jones DBA (2001) The quasi biennial oscillation. Reviews of
- 724 Geophysics, 39:179-229, https://doi.org/10.1029/1999RG000073.
- 725 Cane MA and Sarachik ES (1976) Forced baroclinic ocean motions: 1. Linear equatorial
- unbounded case. Journal of Marine Research 34: 629-665.
- 727 Chane-Ming F, Chen Z and Roux F (2010) Analysis of gravity-waves produced by intense tropical
- 728 cyclones. Annales Geophysicae 28: 531-547. https://doi.org/10.5194/angeo-28-531-2010.
- 729 Chang C and Lim H (1988) Kelvin wave-CISK: A possible mechanism for the 30–50 day
- oscillations. Journal of the Atmospheric Sciences 45: 1709-1720. https://doi.org/10.1175/1520-
- 731 0469(1988)045<1709:KWCAPM>2.0.CO;2.
- 732 Chang CY, Hsiao TC and Chang CC (2013) Tissue Fluorescence Excitation-Emission Matrix
- 733 Analysis Using Multi-Dimensional Ensemble Empirical Mode Decomposition. Transactions of
- 734 Japanese Society for Medical and Biological Engineering 51: R-201.
- 735 <u>https://doi.org/10.11239/jsmbe.51.R-201.</u>
- 736 Chen G and Huang R (2009) Interannual variations in mixed Rossby-gravity waves and their
- 737 impacts on tropical cyclogenesis over the western North Pacific. Journal of Climate 22: 535-549.
- 738 https://doi.org/10.1175/2008JCLI2221.1.
- 739 Chen G and Tam CY (2012) A new perspective on the excitation of low-tropospheric mixed
- Rossby-gravity waves in association with energy dispersion. Journal of the Atmospheric Sciences
- 741 69: 1397-1403. https://doi.org/10.1175/JAS-D-11-0331.1.
- Dee DP, Uppala SM, Simmons AJ et al (2011) The ERA-Interim reanalysis: Configuration and
- 743 performance of the data assimilation system. Quarterly Journal of the royal meteorological society
- 744 137: 553-597. https://doi.org/10.1002/qj.828.
- Dias J and Kiladis GN (2014) Influence of the basic state zonal flow on convectively coupled
- 746 equatorial waves. Geophys. Res. Lett. 41: 6904–6913. https://doi.org/10.1002/2014GL061476.
- Dias J and Kiladis GN (2016) The Relationship between Equatorial Mixed Rossby–Gravity and
- 748 Eastward Inertio- Gravity Waves. Part II. J. Atmos. Sci. 73: 2147-2163.
- 749 https://doi.org/10.1175/JASD-15-0231.1.
- 750 Dickinson M and Molinari J (2002) Mixed Rossby–Gravity Waves and Western Pacific Tropical
- 751 Cyclogenesis. Part I: Synoptic Evolution. Journal of the atmospheric sciences 59: 2183-2196.
- 752 https://doi.org/10.1175/1520-0469(2002)059<2183:MRGWAW>2.0.CO;2.

- 753 Diedhiou A, Janicot S, Viltard A, De Felice P and Laurent H (1999) Easterly wave regimes and
- associated convection over West Africa and tropical Atlantic: results from the NCEP/NCAR and
- 755 ECMWF reanalyses. Climate Dynamics 15: 795-822. https://doi.org/10.1007/s003820050316.
- Dunkerton TJ and Baldwin MP (1995) Observation of 3–6-day meridional wind oscillations over
- 757 the tropical Pacific, 1973–1992: Horizontal structure and propagation. Journal of the atmospheric
- 758 sciences, 52: 1585-1601. https://doi.org/10.1175/1520-
- 759 <u>0469(1995)052<1585:OODMWO>2.0.CO;2.</u>
- Dunkerton TJ, Montgomery MT and Wang Z (2008) Tropical cyclogenesis in a tropical wave
- 761 critical layer: easterly waves. Atmospheric Chemistry and Physics Discussions 8: 11149-11292.
- 762 Emanuel KA, Neelin JD and Bretherton CS (1994) On large-scale circulations in convecting
- atmospheres. Quarterly Journal of the Royal Meteorological Society 120: 1111-1143.
- 764 https://doi.org/10.1002/qj.49712051902.
- Feng J, Wu Z and Liu G (2014) Fast multidimensional ensemble empirical mode decomposition
- 766 using a data compression technique. Journal of Climate 27: 3492-3504.
- 767 https://doi.org/10.1175/JCLI-D-13-00746.1.
- Frank WM and Roundy PE (2006) The role of tropical waves in tropical cyclogenesis. Monthly
- 769 Weather Review 134: 2397-2417. https://doi.org/10.1175/MWR3204.1.
- 770 Gill A (1980) Some simple solutions for heat-induced tropical circulation. Quarterly Journal of the
- 771 Royal Meteorological Society 106: 447-462. https://doi.org/10.1002/qj.49710644905.
- 772 Graham NE and Barnett TP (1987) Sea surface temperature, surface wind divergence, and
- 773 convection over tropical oceans. Science 238: 657-659.
- 774 https://doi.org/10.1126/science.238.4827.657.
- Haertel PT and Kiladis GN (2004) Dynamics of 2-day equatorial waves. Journal of the atmospheric
- 776 sciences 61: 2707-2721. https://doi.org/10.1175/JAS3352.1.
- 777 Held IM and Hou AY (1980) Nonlinear axially symmetric circulations in a nearly inviscid
- atmosphere. Journal of the Atmospheric Sciences 37: 515-533. https://doi.org/10.1175/1520-
- 779 <u>0469(1980)037<0515:NASCIA>2.0.CO;2.</u>
- 780 Hendon HH and Liebmann B (1991) The structure and annual variation of antisymmetric
- 781 fluctuations of tropical convection and their association with Rossby-gravity waves. Journal of the
- 782 atmospheric sciences 48: 2127-2140. https://doi.org/10.1175/1520-
- 783 0469(1991)048<2127:TSAAVO>2.0.CO;2.
- Holton JR (2004) An Introduction to Dynamic Meteorology. Elsevier, Burlington, MA.
- Hou AY and Lindzen RS (1992) The influence of concentrated heating on the Hadley circulation.
- 786 Journal of the Atmospheric Sciences 49: 1233-1241. https://doi.org/10.1175/1520-
- 787 <u>0469(1992)049<1233:TIOCHO>2.0.CO;2.</u>

- Hough SS (1898) On the application of harmonic analysis to the dynamical theory of tides. Part II:
- On the general integration of Laplace's dynamical equations. Philosophical Transactions of the
- 790 Royal Society of London. Series A 191: 139–185.
- Houze RA and Betts AK (1981) Convection in GATE. Reviews of Geophysics 19: 541-576.
- 792 https://doi.org/10.1029/RG019i004p00541.
- Huang NE, Shen Z, Long SR, Wu MC, Shih HH, Zheng Q, Yen N, Tung CC and Liu HH (1998)
- The empirical mode decomposition and the Hilbert spectrum for nonlinear and non-stationary time
- 795 series analysis. Proceedings of the Royal Society of London A: mathematical, physical and
- rgineering sciences 454: 903-995. https://doi.org/10.1098/rspa.1998.0193.
- 797 Huang NE, Shen Z and Long SR (1999) A new view of nonlinear water waves: the Hilbert
- 798 spectrum. Annual review of fluid mechanics 31: 417-457.
- 799 <u>https://doi.org/10.1146/annurev.fluid.31.1.417</u>.
- Huang B, Hu ZZ, Kinter JL, Wu Z and Kumar A (2012) Connection of stratospheric QBO with
- 801 global atmospheric general circulation and tropical SST. Part I: Methodology and composite life
- 802 cycle. Climate dynamics 38: 1-23, https://doi.org/10.1007/s00382-011-1250-7.
- Ji F, Wu Z, Huang J and Chassignet EP (2014) Evolution of land surface air temperature trend.
- Nature Climate Change 4: 462-466. https://doi.org/10.1038/nclimate2223.
- Jin F and Hoskins BJ (1995) The direct response to tropical heating in a baroclinic atmosphere.
- 306 Journal of the atmospheric sciences 52: 307-319. https://doi.org/10.1175/1520-
- 807 0469(1995)052<0307:TDRTTH>2.0.CO;2.
- Kalnay E, Kanamitsu M, Kistler R et al. (1996) The NCEP/NCAR 40-year reanalysis project.
- Bulletin of the American meteorological Society 77: 437-471. https://doi.org/10.1175/1520-
- 810 0477(1996)077<0437:TNYRP>2.0.CO;2.
- Kikuchi K and Wang B (2010) Spatiotemporal wavelet transform and the multiscale behavior of
- 812 the Madden-Julian oscillation. Journal of Climate 23: 3814-3834.
- 813 https://doi.org/10.1175/2010JCLI2693.1.
- Kiladis GN and Weickmann KM (1992) Extratropical forcing of tropical Pacific convection during
- 815 northern winter. Monthly Weather Review 120: 1924-1939. https://doi.org/10.1175/1520-
- 816 0493(1992)120<1924:EFOTPC>2.0.CO;2.
- Kiladis GN and Weickmann KM (1992) Circulation anomalies associated with tropical convection
- during northern winter. Monthly Weather Review 120: 1900-1923. https://doi.org/10.1175/1520-
- 819 0493(1992)120<1900:CAAWTC>2.0.CO;2.
- 820 Kiladis GN, Wheeler MC, Haertel PT66295, Straub KH and Roundy PE (2009) Convectively
- coupled equatorial waves. Reviews of Geophysics 47. https://doi.org/10.1029/2008RG000266.

- Kiladis GN, Dias J and Gehne M (2016) The Relationship between Equatorial Mixed Rossby-
- 823 Gravity and Eastward Inertio-Gravity Waves. Part I. J. Atmos. Sci. 73: 2123-2145.
- 824 https://doi.org/10.1175/JAS-D-15-0230.1.
- Kistler R, Kalnay E, Collins W et al. (2001) The NCEP-NCAR 50-year reanalysis: Monthly means
- 826 CD-ROM and documentation. Bulletin of the American Meteorological society 82: 247-267.
- 827 Kumar KK, Rajagopalan B and Cane MA (1999) On the weakening relationship between the
- 828 Indian monsoon and ENSO Science 284: 2156-2159.
- 829 https://doi.org/10.1126/science.284.5423.2156.
- Li H and Misra V (2014) Global seasonal climate predictability in a two tiered forecast system.
- 831 Part II: boreal winter and spring seasons. Climate Dynamics 42: 1449-1468.
- 832 <u>https://doi.org/10.1007/s00382-013-1813-x</u>.
- Lindzen RS (1974) Wave-CISK in the tropics. Journal of the Atmospheric Sciences 31: 156-179.
- https://doi.org/10.1175/1520-0469(1974)031<0156:WCITT>2.0.CO;2.
- Lindzen RS and Tsay CY (1975) Wave structure of the tropical stratosphere over the Marshall
- Islands area during 1 April–1 July 1958. Journal of the Atmospheric Sciences 32: 2008-2021.
- 837 <u>https://doi.org/10.1175/1520-0469(1975)032<2008:WSOTTS>2.0.CO;2.</u>
- Lindzen RS and Holton JR (1968) A theory of the quasi-biennial oscillation. Journal of the
- 839 Atmospheric Sciences 25: 1095-1107. https://doi.org/10.1175/1520-
- 840 0469(1968)025<1095:ATOTQB>2.0.CO;2.
- Liebmann B and Hendon HH (1990) Synoptic-scale disturbances near the equator. Journal of the
- 842 Atmospheric Sciences 47: 1463-1479. https://doi.org/10.1175/1520-
- 843 0469(1990)047<1463:SSDNTE>2.0.CO:2.
- McDonald AJ, Baumgaertner AJG, Fraser GJ, George SE and Marsh S (2007) Empirical Mode
- Decomposition of the atmospheric wave field. Annales Geophysicae 25: 375-384.
- Magaña V and Yanai M (1995) Mixed Rossby–gravity waves triggered by lateral forcing. Journal
- 847 of the Atmospheric Sciences 52: 1473-1486. https://doi.org/10.1175/1520-
- 848 0469(1995)052<1473:MRWTBL>2.0.CO;2.
- Mapes BE and Houze RA Jr. (1995) Diabatic divergence profiles in western Pacific mesoscale
- 850 convective systems. Journal of the Atmospheric Sciences 52: 1807-1828.
- 851 https://doi.org/10.1175/1520-0469(1995)052<1807:DDPIWP>2.0.CO;2.
- Maruyama T (1969) Long-Term Behaviour of Kelvin Waves and Mixed Rassby Gravity Waves.
- 853 Journal of the Meteorological Society of Japan 47: 245-254.
- 854 https://doi.org/10.2151/jmsj1965.47.4 245.
- 855 Maruyama T (1991) Annual and OBO-synchronized variations of lower-stratospheric equatorial
- wave activity over Singapore during 1961-1989. Journal of the Meteorological Society of Japan
- 857 69: 219-232. https://doi.org/10.2151/jmsj1965.69.2 219.

- Matsui T, Chern JD, Tao WK, Lang S, Satoh M, Hashino T and Kubota T (2016) On the Land-
- Ocean Contrast of Tropical Convection and Microphysics Statistics Derived from TRMM Satellite
- 860 Signals and Global Storm-Resolving Models. Journal of Hydrometeorology 17: 1425-1445.
- 861 https://doi.org/10.1175/JHM-D-15-0111.1.
- Matsuno T (1966) Quasi-geostrophic motions in the equatorial area. Journal of the Meteorological
- 863 Society of Japan 44: 25-43. https://doi.org/10.2151/jmsj1965.44.1 25.
- Meyers SD, Kelly BG and O'Brien JJ (1993) An introduction to wavelet analysis in oceanography
- and meteorology: With application to the dispersion of Yanai waves. Monthly Weather Review
- 866 121: 2858-2866. https://doi.org/10.1175/1520-0493(1993)121<2858:AITWAI>2.0.CO;2.
- Nakamura T, Aono T, Tsuda T, Admiranto AG and Achmad E (2003) Mesospheric gravity waves
- 868 over a tropical convective region observed by OH airglow imaging in Indonesia. Geophysical
- 869 Research Letters 30. https://doi.org/10.1029/2003GL017619.
- Neelin JD and Held IM (1987) Modeling tropical convergence based on the moist static energy
- 871 budget. Monthly Weather Review 115: 3-12. https://doi.org/10.1175/1520-
- 872 <u>0493(1987)115<0003:MTCBOT>2.0.CO;2.</u>
- 873 Ogrosky HR and Stechmann SN (2016) Identifying convectively coupled equatorial waves using
- 874 theoretical wave eigenvectors. Monthly Weather Review 144: 2235-2264.
- 875 <u>https://doi.org/10.1175/MWR-D-15-0292.1</u>.
- Petersen WA and Rutledge SA (2001) Regional variability in tropical convection: Observations
- 877 from TRMM. Journal of climate 14: 3566-3586. https://doi.org/10.1175/1520-
- 878 0442(2001)014<3566:RVITCO>2.0.CO;2.
- Pfister L, Chan KR, Bui TP, Bowen S, Legg M, Gary B, Kelly K, Proffitt M and Starr W (1993)
- 880 Gravity waves generated by a tropical cyclone during the STEP tropical field program: A case
- 881 study. Journal of Geophysical Research: Atmospheres 98: 8611-8638.
- 882 https://doi.org/10.1029/92JD01679.
- Raymond DJ (2000) Thermodynamic control of tropical rainfall. Quarterly Journal of the Royal
- Meteorological Society 126: 889-898, https://doi.org/10.1002/qi.49712656406.
- Raymond DJ, Sessions SL, Sobel AH, and Fuchs Ž (2009) The mechanics of gross moist stability.
- Journal of Advances in Modeling Earth Systems 1. https://doi.org/10.3894/JAMES.2009.1.9.
- Rojas A, Górriz JM, Ramírez J, Gallix A and Illán IA (2012) Empirical Mode Decomposition as
- a feature extraction method for Alzheimer's Disease Diagnosis. Nuclear Science Symposium and
- 889 Medical Imaging Conference (NSS/MIC) IEEE: 3909-3913
- 890 <u>https://doi.org/10.1109/NSSMIC.2012.6551897.</u>
- Rossby CG (1939) Relation between variations in the intensity of the zonal circulation of the
- atmosphere and the displacements of the semi-permanent centers of action. Journal of Marine
- 893 Research 2: 38-55.

- Roundy PE (2012) Observed structure of convectively coupled waves as a function of equivalent
- depth: Kelvin waves and the Madden–Julian oscillation. Journal of the Atmospheric Sciences 69:
- 896 2097-2106. https://doi.org/10.1175/JAS-D-12-03.1.
- 897 Schneider EK and Lindzen RS (1977) Axially symmetric steady-state models of the basic state for
- instability and climate studies. Part I. Linearized calculations. Journal of the Atmospheric Sciences
- 899 34: 263-279. https://doi.org/10.1175/1520-0469(1977)034<0263:ASSSMO>2.0.CO;2.
- 900 Schneider T (2006) The general circulation of the atmosphere. Annual Review of Earth and
- 901 Planetary Sciences 34: 655-688. https://doi.org/10.1146/annurev.earth.34.031405.125144.
- 902 Straus DM and Lindzen RS (2000) Planetary-scale baroclinic instability and the MJO. Journal of
- 903 the Atmospheric Sciences 57: 3609-3626. https://doi.org/10.1175/1520-
- 904 0469(2000)057<3609:PSBIAT>2.0.CO;2.
- 905 Straub KH and Kiladis GN (2003) Extratropical forcing of convectively coupled Kelvin waves
- 906 during austral winter. Journal of the Atmospheric Sciences 60: 526-543.
- 907 https://doi.org/10.1175/1520-0469(2003)060<0526:EFOCCK>2.0.CO;2.
- 908 Sui CH and Lau KM (1989) Origin of low-frequency (intraseasonal) oscilliations in the tropical
- atmosphere. Part II: Structure and propagation of mobile wave-CISK modes and their modification
- 910 by lower boundary forcings. Journal of the Atmospheric Sciences 46: 37-56
- 911 <u>https://doi.org/10.1175/1520-0469(1989)046<0037:OOLFOI>2.0.CO;2.</u>
- Takayabu YN and Nitta T (1993) 3-5 day-period disturbances coupled with convection over the
- 913 tropical Pacific Ocean. Journal of the Meteorological Society of Japan 71: 221-246.
- 914 https://doi.org/10.2151/jmsj1965.71.2 221.
- Takayabu YN (1994) Large-scale cloud disturbances associated with equatorial waves. Journal of
- 916 the Meteorological Society of Japan 72: 433-449. https://doi.org/10.2151/jmsj1965.72.3 433.
- 917 Takayabu YN (1994) Large-scale cloud disturbances associated with equatorial waves. Part II:
- Westward-propagating inertio-gravity waves. Journal of the Meteorological Society of Japan 72:
- 919 451-465. https://doi.org/10.2151/jmsj1965.72.3 451.
- 920 Tao SY (1987) A review of recent research on the east Asia summer monsoon in China. Monsoon
- 921 Meteorology 50-92.
- 922 Tsuda T, Murayama Y, Wiryosumarto H, Harijono SWB and Kato S (1994) Radiosonde
- observations of equatorial atmosphere dynamics over Indonesia: 1. Equatorial waves and diurnal
- 924 tides. Journal of Geophysical Research: Atmospheres 99: 10491-10505.
- 925 https://doi.org/10.1029/94JD00355.
- 926 Wallace JM and Kousky VE (1968) Observational evidence of Kelvin waves in the tropical
- stratosphere. Journal of the Atmospheric Sciences 25: 900-907. https://doi.org/10.1175/1520-
- 928 0469(1968)025<0900:OEOKWI>2.0.CO;2.

- 929 Wallace JM (1971) Spectral studies of tropospheric wave disturbances in the tropical western
- 930 Pacific. Reviews of Geophysics 9: 557-612. https://doi.org/10.1029/RG009i003p00557.
- 931 Wallace JM and Chang CP (1969) Spectrum analysis of large-scale wave disturbances in the
- 932 tropical lower troposphere. Journal of the Atmospheric Sciences 26: 1010-1025.
- 933 https://doi.org/10.1175/1520-0469(1969)026<1010:SAOLSW>2.0.CO;2.
- Wang B and Rui H (1990) Dynamics of the coupled moist Kelvin–Rossby wave on an equatorial
- 935 β-plane. Journal of the Atmospheric Sciences 47: 397-413. https://doi.org/10.1175/1520-
- 936 0469(1990)047<0397:DOTCMK>2.0.CO;2.
- Wang P, Clemens S, Beaufort L, Braconnot P, Ganssen G, Jian Z, Kershaw P and Samthein M
- 938 (2005) Evolution and variability of the Asian monsoon system: state of the art and outstanding
- 939 issues. Quaternary Science Reviews 24: 595-629. https://doi.org/10.1016/j.quascirev.2004.10.002.
- 940 Webster PJ and Yang S (1992) Monsoon and ENSO: Selectively interactive systems. Quarterly
- 941 Journal of the Royal Meteorological Society 118: 877-926.
- 942 https://doi.org/10.1002/qj.49711850705.
- Wheeler M and Kiladis GN (1999) Convectively coupled equatorial waves: Analysis of clouds
- and temperature in the wavenumber-frequency domain. Journal of the Atmospheric Sciences 56:
- 945 374-399. <a href="https://doi.org/10.1175/1520-0469(1999)056<0374:CCEWAO>2.0.CO;2">https://doi.org/10.1175/1520-0469(1999)056<0374:CCEWAO>2.0.CO;2.
- Wheeler M and Kiladis GN and Webster PJ (2000) Large-scale dynamical fields associated with
- onvectively coupled equatorial waves. Journal of the Atmospheric Sciences 57: 613-640.
- 948 https://doi.org/10.1175/1520-0469(2000)057<0613:LSDFAW>2.0.CO;2.
- 949 Whitcher B, Guttorp P and Percival DB (2000) Wavelet analysis of covariance with application to
- atmospheric time series. Journal of Geophysical Research: Atmospheres 105: 14941-14962.
- 951 https://doi.org/10.1029/2000JD900110.
- 952 Wu Z, Sarachik ES and Battisti DS (2000) Vertical Structure of Convective Heating and the Three-
- 953 Dimensional Structure of the Forced Circulation on an Equatorial Beta Plane. Journal of the
- 954 Atmospheric Sciences 57: 2169–2187. https://doi.org/10.1175/1520-
- 955 0469(2000)057<2169:VSOCHA>2.0.CO;2.
- 956 Wu Z, Battisti DS and Sarachik ES (2000) Rayleigh Friction, Newtonian Cooling, and the Linear
- 957 Response to Steady Tropical Heating. Journal of the Atmospheric Sciences 57: 1937–1957.
- 958 https://doi.org/10.1175/1520-0469(2000)057<1937:RFNCAT>2.0.CO;2.
- 959 Wu Z, Sarachik ES and Battisti DS (2001) Thermally Driven Tropical Circulations under Rayleigh
- 960 Friction and Newtonian Cooling: Analytic Solutions. Journal of the Atmospheric Sciences 58:
- 961 724–741. https://doi.org/10.1175/1520-0469(2001)058<0724:TDTCUR>2.0.CO;2.
- 962 Wu Z (2003) A Shallow CISK, Deep Equilibrium Mechanism for the Interaction between Large-
- 963 Scale Convection and Large-Scale Circulations in the Tropics. Journal of the Atmospheric
- 964 Sciences 60: 377–392. https://doi.org/10.1175/1520-0469(2003)060<0377:ASCDEM>2.0.CO;2.

- Wu Z and Huang NE (2004) A study of the characteristics of white noise using the empirical mode
- decomposition method. Proceedings of the Royal Society of London A: Mathematical, Physical
- and Engineering Sciences 460: 1597-1611. https://doi.org/10.1098/rspa.2003.1221.
- 968 Wu Z, Huang NE and Chen X (2009) The multi-dimensional ensemble empirical mode
- 969 decomposition method. Advances in Adaptive Data Analysis 1: 339-372.
- 970 https://doi.org/10.1142/S1793536909000187.
- 971 Wu Z and Huang NE (2009) Ensemble empirical mode decomposition: a noise-assisted data
- 972 analysis method. Advances in Adaptive Data Analysis 1: 1–41.
- 973 https://doi.org/10.1142/S1793536909000047.
- Wu Z and Huang NE (2010) On the filtering properties of the empirical mode decomposition.
- 975 Advances in Adaptive Data Analysis 2: 397-414. https://doi.org/10.1142/S1793536910000604.
- 976 Wu Z, Huang NE, Wallace JM, Smoliak BV and Chen X (2011) On the time-varying trend in
- global-mean surface temperature. Climate dynamics 37: 759-773. https://doi.org/10.1007/s00382-
- 978 011-1128-8.
- 979 Yan TQ, Liu SF, and Zhou CX (2011) Palmprint Recognition with MEEMD and Statistically
- 980 Independent Coefficients ICA. In: Huang DS., Gan Y., Bevilacqua V., Figueroa J.C. (eds)
- Advanced Intelligent Computing. ICIC 2011. Lecture Notes in Computer Science 6838. Springer,
- 982 Berlin, Heidelberg, https://doi.org/10.1007/978-3-642-24728-6 53.
- 983 Yanai M and Maruyama T (1966) Stratospheric Wave Disturbances Propagating over the
- 984 Equatorial Pacific. Journal of the Meteorological Society of Japan 44: 291-294.
- 985 https://doi.org/10.2151/jmsj1965.44.5 291.
- Yanai M, Maruyama T, Nitta T and Hayashi Y (1968) Power spectra of large-scale disturbances
- over the tropical Pacific. Journal of the Meteorological Society of Japan 46: 308-323.
- 988 https://doi.org/10.2151/jmsj1965.46.4 308.
- 989 Yang GY, Hoskins B and Slingo J (2003) Convectively coupled equatorial waves: A new
- 990 methodology for identifying wave structures in observational data. Journal of the Atmospheric
- 991 Sciences, 60: 1637-1654. https://doi.org/10.1175/1520-
- 992 0469(2003)060<1637:CCEWAN>2.0.CO;2.
- 993 Yao Y, Sfarra S, Ibarra-Castanedo C, You R and Maldague XPV (2017) The multi-dimensional
- 994 ensemble empirical mode decomposition (MEEMD). Journal of Thermal Analysis and
- 995 Calorimetry 128: 1841-1858. https://doi.org/10.1007/s10973-016-6082-6.
- 296 Zhang C and Webster PJ (1992) Laterally forced equatorial perturbations in a linear model. Part I:
- 997 Stationary transient forcing. Journal of the Atmospheric Sciences 49: 585-607.
- 998 https://doi.org/10.1175/1520-0469(1992)049<0585:LFEPIA>2.0.CO;2.
- 299 Zhang Y, Wallace JM and Battisti DS (1997) ENSO-like interdecadal variability: 1900–93.
- 1000 Journal of Climate 10: 1004-1020. https://doi.org/10.1175/1520-
- 1001 0442(1997)010<1004:ELIV>2.0.CO;2.

Zhu X, Shen Z, Eckermann SD, Bittner M, Hirota I and Yee JH (1997) Gravity wave characteristics in the middle atmosphere derived from the empirical mode decomposition method. Journal of Geophysical Research: Atmospheres 102: 16545-16561. https://doi.org/10.1029/97JD01139.

- FIG. 1 Fourier spectra of MRG wave fields. a) A spatiotemporally homogeneous MRG wave field; b) the Fourier spectrum of the wave field displayed in a); c) a spatiotemporally local MRG wave field; and d) The same as b) but for wave filed displayed in c). In panels b) and d), red curves correspond to MRG wave dispersion relationship with equivalent depth 25 m, black curves 50 m, and green curves 250 m. The displayed spectra are divided by the total energy of each corresponding individual wave field to make the displayed color in b) and d) with unit of percentage
- FIG. 2 The intuition behind EMD. The blue curve C is a pure oscillatory component (monocomponent) with its amplitude a(t) being given as the yellow curve at the top; the red curve is the background slower varying component R; and the black curve is S(t), the sum of R and C. Among the bottom group curves, the yellow curves are R(t) + a(t) and R(t) - a(t), respectively
 - FIG. 3 Spatial coherence and temporal locality of EEMD decomposition. a) The original meridional wind data (original, $X_{s,t}$) and successive EEMD components (the 1st mode to the 5th mode, $C_{i,s,t}$) at neighboring grid points. The blue curves correspond to the grid point (102.5°E,0°) and red curves to the grid point (100°E,0°). b) The original meridional wind data (original, $X_{s,t}$) and successive EEMD components (the 1st mode to the 5th mode, $C_{i,s,t}$) at the same grid point but by different temporal lengths. Blue curves correspond to the range of the 50th to the 99th day, red curves the 50th day to the 97th day and black curves the 50th day to the 95th day
 - FIG. 4 MEEMD decomposition of multi-dimensional meridional wind data. a) The meridional winds along the Equator between 160°E and 170°E within temporal range of the first 50 days in 2002; b) f) the MEEMD components from the 1st mode to the 5th mode, respectively. The color schemes for different panels are different (not shown). The color schemes are the same for all panels (at the far right) except for a; for which the colorbar is placed immediately to its right-hand-side
 - FIG. 5 Synthetic data experiments testing the impacts of locality to spectra analysis method and the efficiency of the MEEMD method. a) MRG wave field with high locality, the same as in Fig. 1c, but only the first 150 time steps are displayed here; b) marginal wavenumber-frequency spectrum of the MRG wave field in a); c) the noise contaminated MRG wave field; d) marginal wavenumber-frequency spectrum of the noise contaminated MRG wave field in c); e) MRG wave field obtained from MEEMD method; and e) the marginal wavenumber-frequency spectrum of the MEEMD method decomposed MRG waves field in e). The color of curves and shaded color schemes are the same as those in Fig. 1
 - FIG. 6 Longitude-time profile (Hovmöller Diagram) of 850 hPa equatorial meridional wind from the 4th MEEMD mode. The shaded colors represent the values of meridional wind strength with positive values (northward) in red colors and negative values (southward) in blue colors, while the x-axis and y-axis are longitude and time, respectively. The unit in the color scheme is ms⁻¹. The red box indicates the spatiotemporal location of the MRG event shown in Fig.7, the blue box in Figs.9a-9e, the green box Figs.9f-9j, and the black box in Figs.9k-9o

FIG. 7 The evolution of an MRG wave event example over the tropical western Pacific Ocean region obtained from different filters. a) The original meridional wind field; b) meridional wind from the fourth MEEMD component, c) the meridional from Fourier filter with band 6-12 days, zonal wavenumber 6-18. The unit of colormap is m/s

- FIG. 8 Comparison of diagnosed MRG wave pattern over the western Pacific Ocean region with theoretically calculated one. a-j) The MEEMD extracted daily MRG wave structures from Oct. 8 to Oct. 17, with horizontal winds in vector form and geopotential shaded; k) the same as a-j but for theoretical MRG wave from a non-dimensionalized shallow water system; and l) the same as c but enlarged for comparison with k. The amplitude of wind is plotted at the lower-right corner of panel j
- FIG. 9 The same as Fig. 7 but for different tropical regions and temporal ranges. a) e), tropical Indian Ocean region between 7 November and 11 November, respectively; f) g), tropical eastern Pacific region between 29 September and 3 October, respectively; k) o), tropical Atlantic Ocean region between 1 August and 5 August, respectively
 - FIG. 10 Marginal zonal wavenumber-frequency spectra of global MRG waves from MEEMD components 3 and 4. a) MRG wave spectrum for year 2002; and b) MRG wave spectrum for years 1979-2013. The color scheme represents the summed energy projected onto the small bin of the zonal wavenumber-frequency domain. The solid curves are theoretical MRG wave dispersion relationship for equivalent depths (blue 1 m; pink 5m; red 25m; green 50m; and black 100 m). The dashed black curve is the theoretical dispersion relationship for n = 1 inertio-gravity wave with equivalent depth 5m. The green, red and pink dashed curves are theoretical n = 1 equatorial Rossby wave dispersion relationship for different equivalent depths (pink 5m; red 25m; and green 50m)
 - FIG. 11 The same as Fig.10b but for different regions for the period 1979-2013: a) Indian Ocean, b) western Pacific, c) eastern Pacific, and d) Atlantic Ocean
 - FIG. A1 The phase speed and group velocity of an MRG wave event. a) the sequential meridional winds along Equator from MEEMD component 4 for Oct. 8 to 12 of 2002, and b) their corresponding EEMD component 2's. The red curves are the envelops of EEMD components 2's. The blue dashed line indicates the phase speed and the red dashed line the group velocity
 - FIG. A2 The MEEMD 4th component of the meridional wind at the Equator (the same as Fig. 6) and the fitted amplitude. The values are indicated by the corresponding colorbars with a unit of ms⁻¹. In the right panel, regions with amplitude less than 1.5 ms⁻¹ is left blank

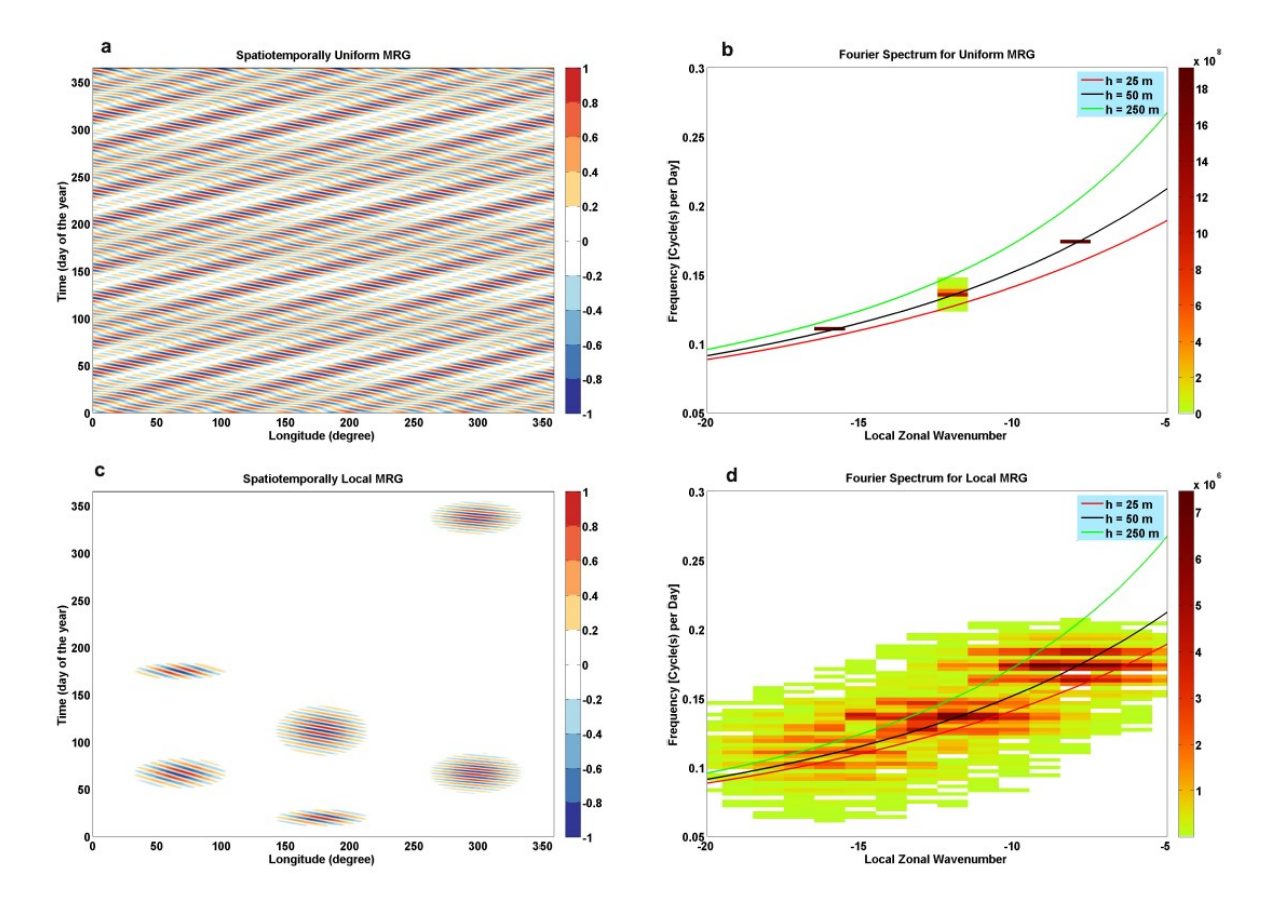


FIG. 1 Fourier spectra of MRG wave fields. a) A spatiotemporally homogeneous MRG wave field; b) the Fourier spectrum of the wave field displayed in a); c) a spatiotemporally local MRG wave field; and d) The same as b) but for wave filed displayed in c). In panels b) and d), red curves correspond to MRG wave dispersion relationship with equivalent depth 25 m, black curves 50 m, and green curves 250 m. The displayed spectra are divided by the total energy of each corresponding individual wave field to make the displayed color in b) and d) with unit of percentage

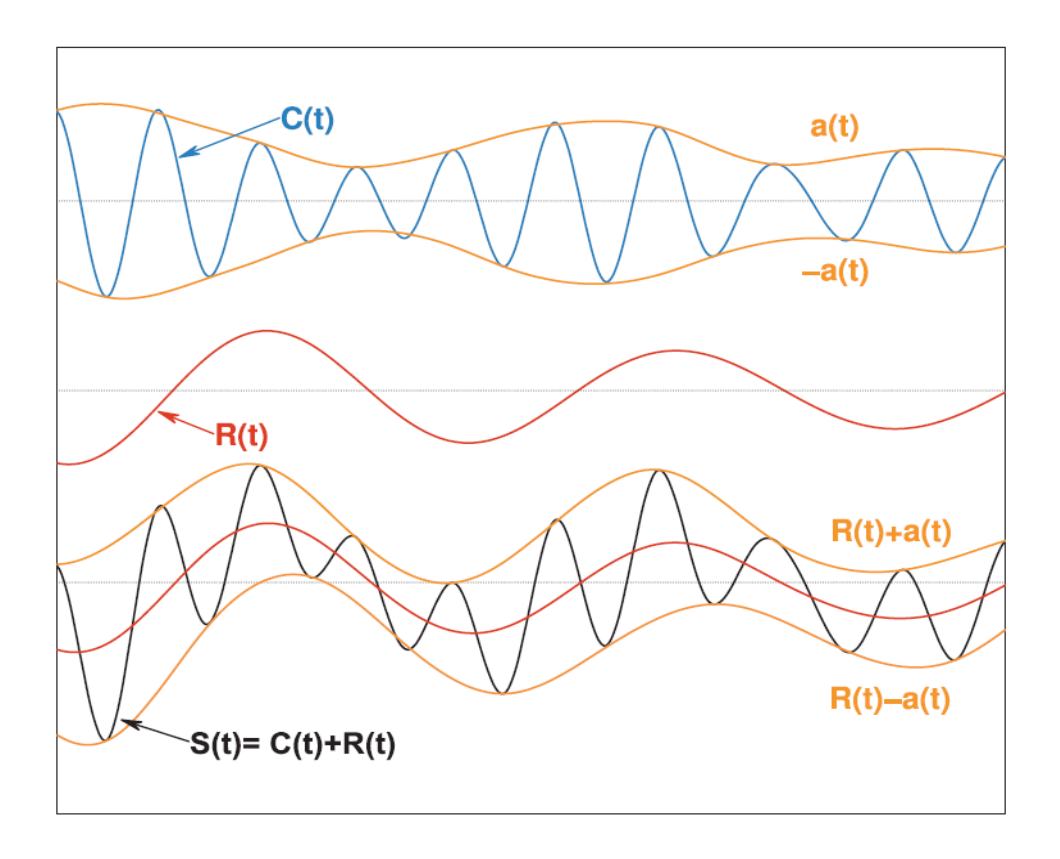


FIG. 2 The intuition behind EMD. The blue curve C is a pure oscillatory component (monocomponent) with its amplitude a(t) being given as the orange curve at the top; the red curve is the background slower varying component R; and the black curve is S(t), the sum of R and C. Among the bottom group curves, the orange curves are R(t) + a(t) and R(t) - a(t), respectively

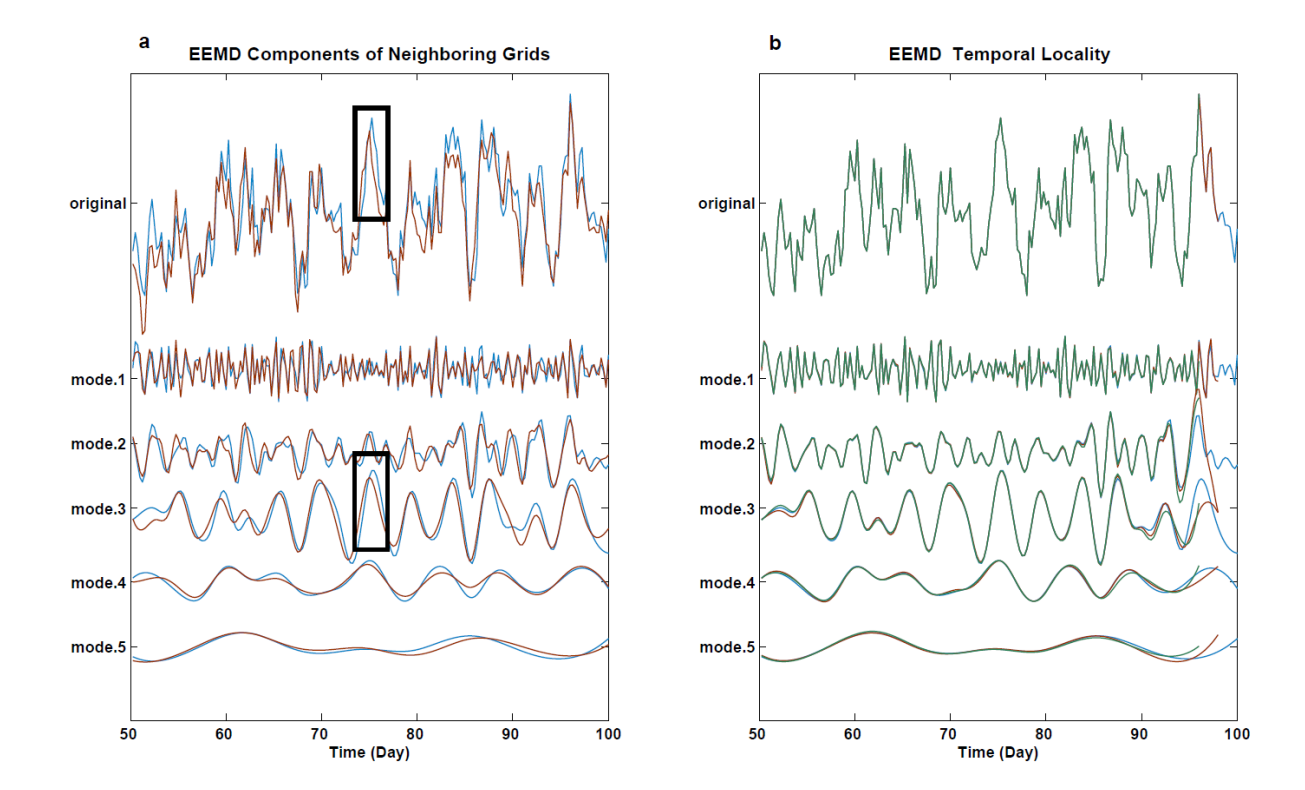


FIG. 3 Spatial coherence and temporal locality of EEMD decomposition. a) The original meridional wind data (original, $X_{s,t}$) and successive EEMD components (the 1st mode to the 5th mode, $C_{i,s,t}$) at neighboring grid points. The blue curves correspond to the grid point (177.5°E,0°) and red curves to the grid point (180°,0°). b) The original meridional wind data (original, $X_{s,t}$) and successive EEMD components (the 1st mode to the 5th mode, $C_{i,s,t}$) at the same grid point but by different temporal lengths. Blue curves correspond to the range of the 50th to the 99th day, red curves the 50th day to the 97th day and black curves the 50th day to the 95th day

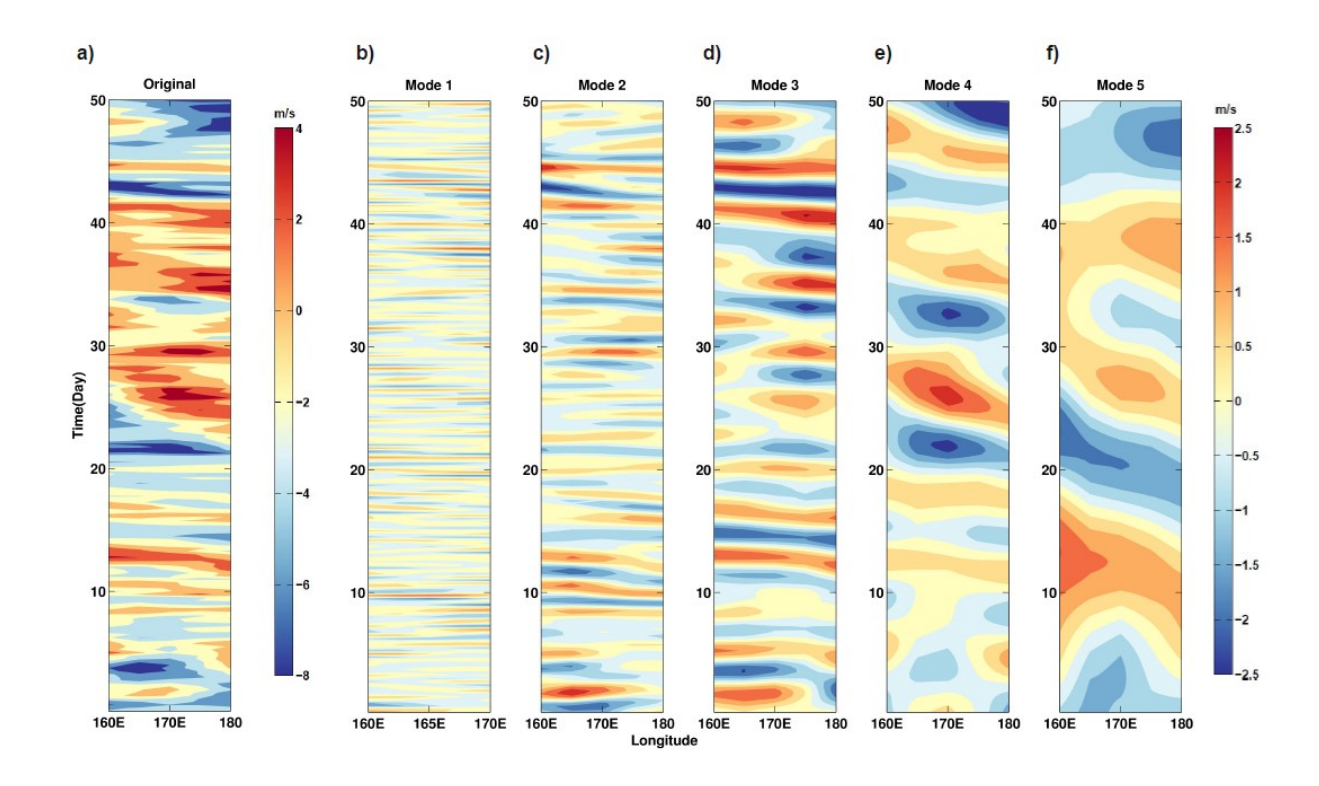


FIG. 4 MEEMD decomposition of multi-dimensional meridional wind data at the equator. a) The meridional winds along the Equator between 160°E and 180° within temporal range of the first 50 days in 2002; **b)** - **f)** the MEEMD components from the 1st mode to the 5th mode, respectively. The color schemes are the same for all panels (at the far right) except for **a**; for which the colorbar is placed immediately to its right-hand-side

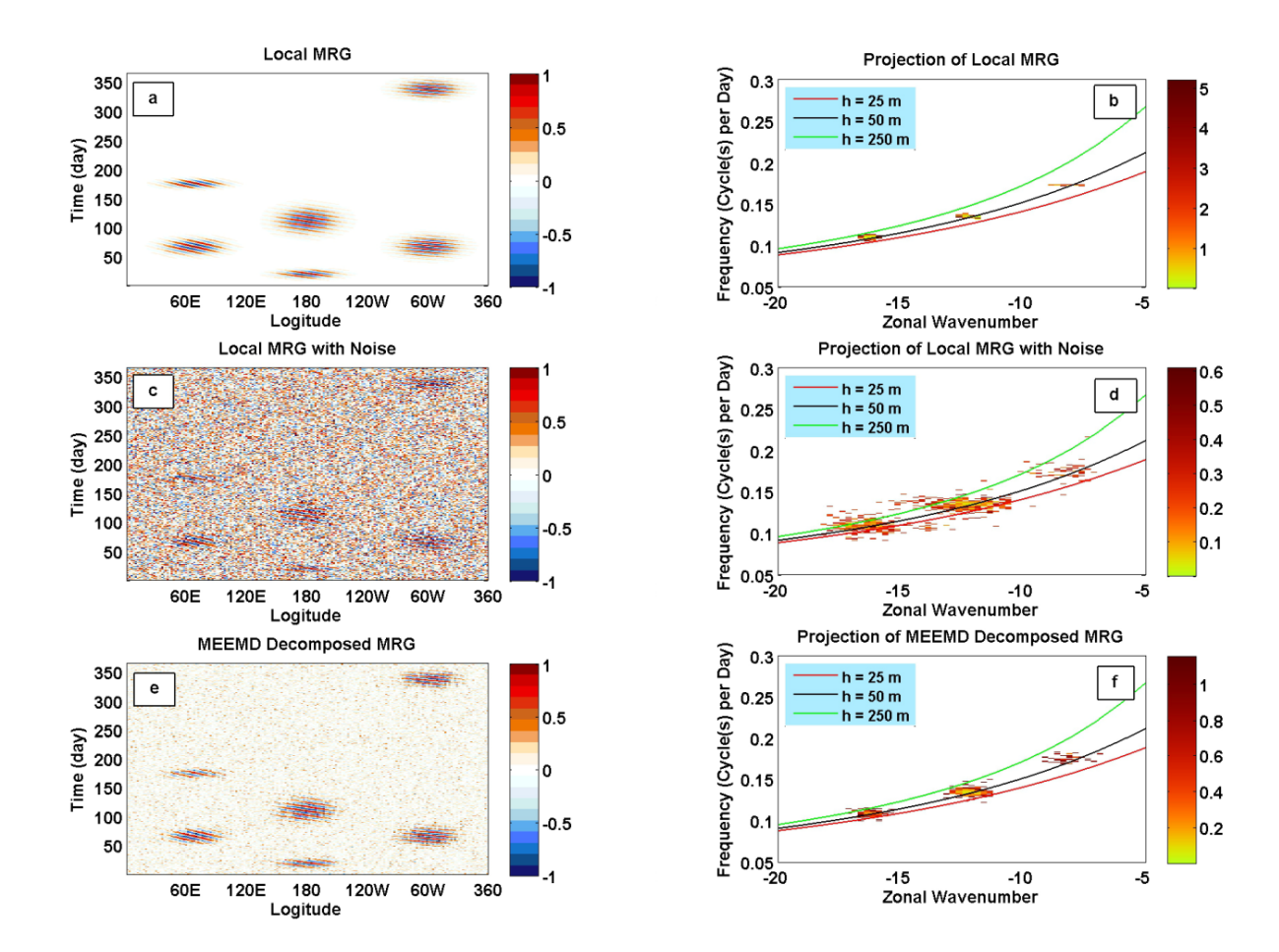


FIG. 5 Synthetic data experiments testing the impacts of locality to spectra analysis method and the efficiency of the MEEMD method. a) MRG wave field with high locality, the same as in Fig. 1c, but only the first 150 time steps are displayed here; b) marginal wavenumber-frequency spectrum of the MRG wave field in a); c) the noise contaminated MRG wave field; d) marginal wavenumber-frequency spectrum of the noise contaminated MRG wave field in c); e) MRG wave field obtained from MEEMD method; and e) the marginal wavenumber-frequency spectrum of the MEEMD method decomposed MRG waves field in e). The color of curves and shaded color schemes are the same as those in Fig. 1

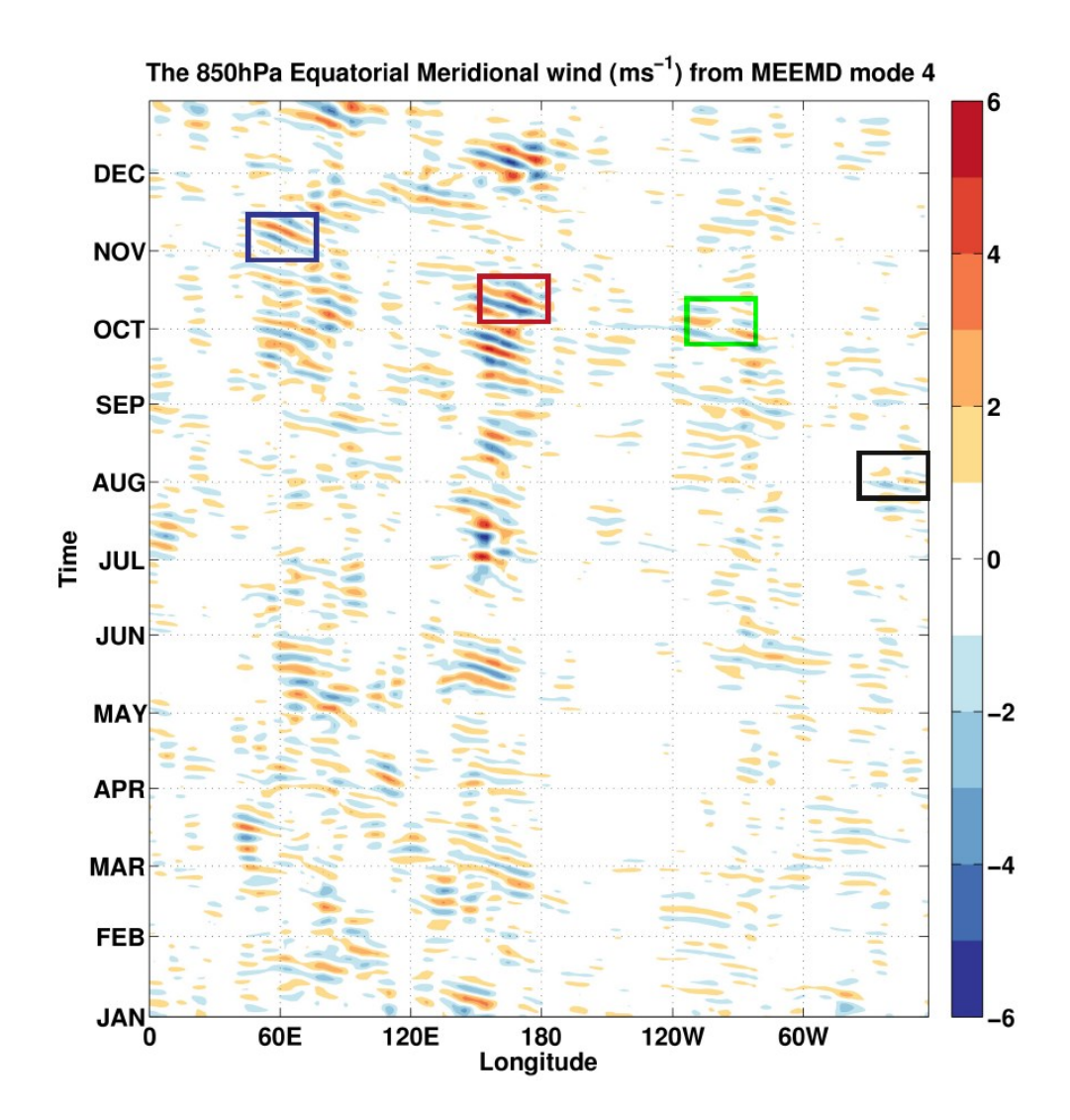


FIG. 6 Longitude-time profile (Hovmöller Diagram) of 850 hPa equatorial meridional wind at the equator from the 4th MEEMD mode. The shaded colors represent the values of meridional wind strength with positive values (northward) in red colors and negative values (southward) in blue colors, while the x-axis and y-axis are longitude and time, respectively. The unit in the color scheme is ms⁻¹. The red box indicates the spatiotemporal location of the MRG event shown in Fig.7, the blue box in Figs.9a-9e, the green box Figs.9f-9j, and the black box in Figs.9k-9o

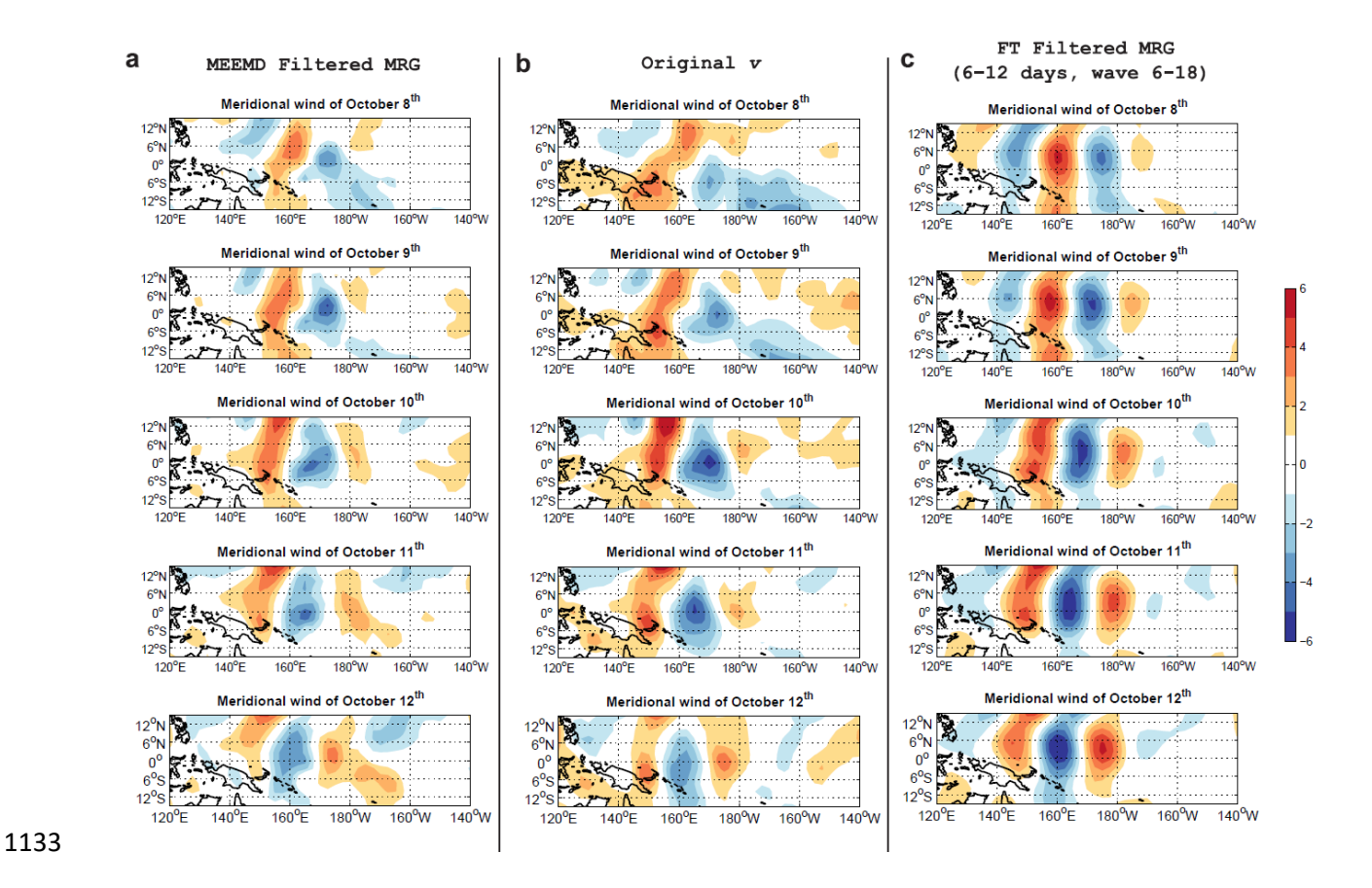


FIG. 7 The evolution of an MRG wave event example over the tropical western Pacific Ocean region obtained from different filters. a) meridional wind from the fourth MEEMD component; The original meridional wind field; b) The original meridional wind field; meridional wind from the fourth MEEMD component, and c) the meridional from Fourier filter with band 6-12 days, zonal wavenumber 6-18. The unit of colormap is m/s.



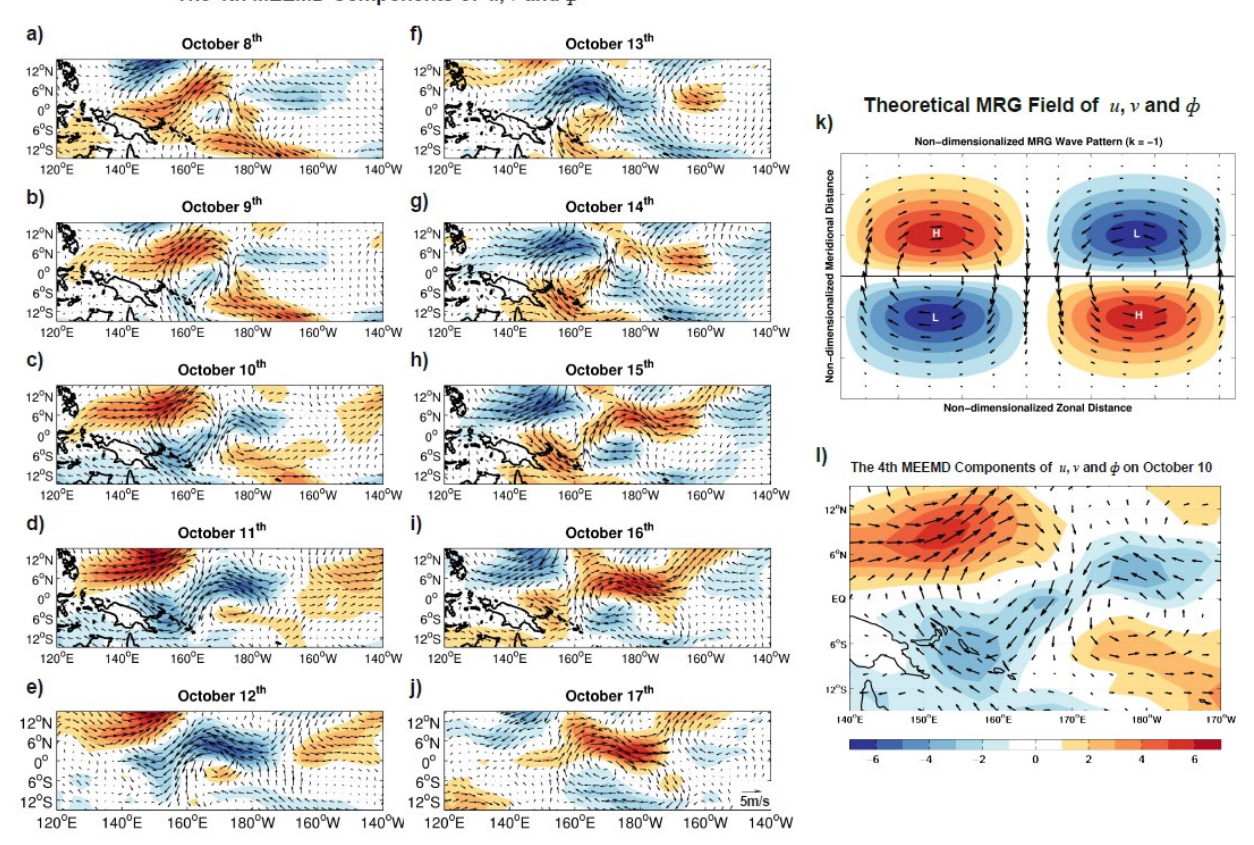


FIG. 8 Comparison of diagnosed MRG wave pattern over the western Pacific Ocean region with theoretically calculated one. a-j) The MEEMD extracted daily MRG wave structures from Oct. 8 to Oct. 17, with horizontal winds in vector form and geopotential shaded; k) the same as a-j but for theoretical MRG wave from a non-dimensionalized shallow water system; and l) the same as c but enlarged for comparison with k. The amplitude of wind is plotted at the lower-right corner of panel j

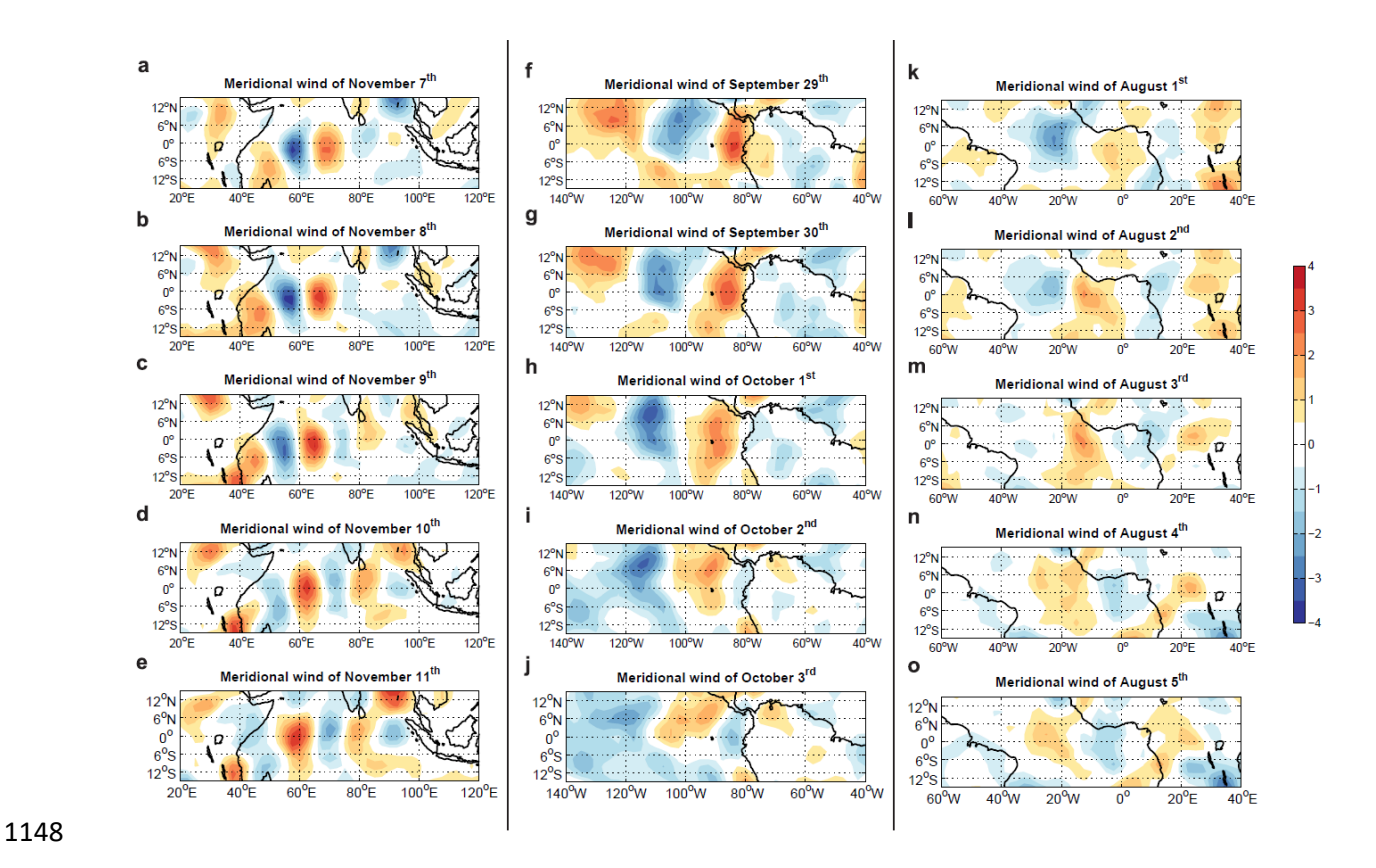
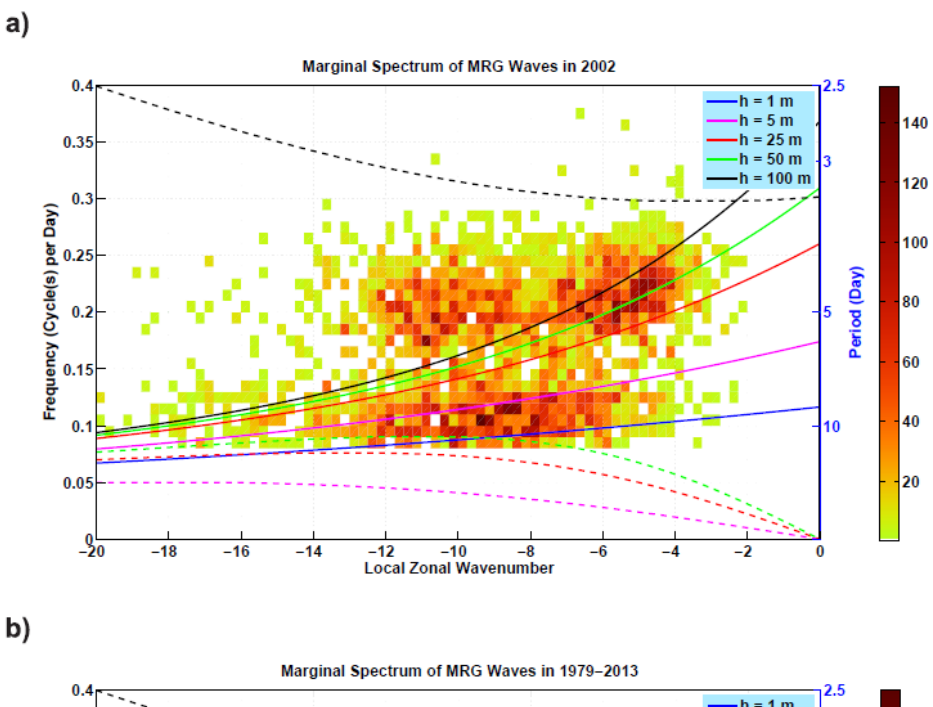


FIG. 9 The same as Fig. 7ab but for different tropical regions and temporal ranges. a) - e), tropical Indian Ocean region between 7 November and 11 November, respectively; f) - g), tropical eastern Pacific region between 29 September and 3 October, respectively; k) - o), tropical Atlantic Ocean region between 1 August and 5 August, respectively



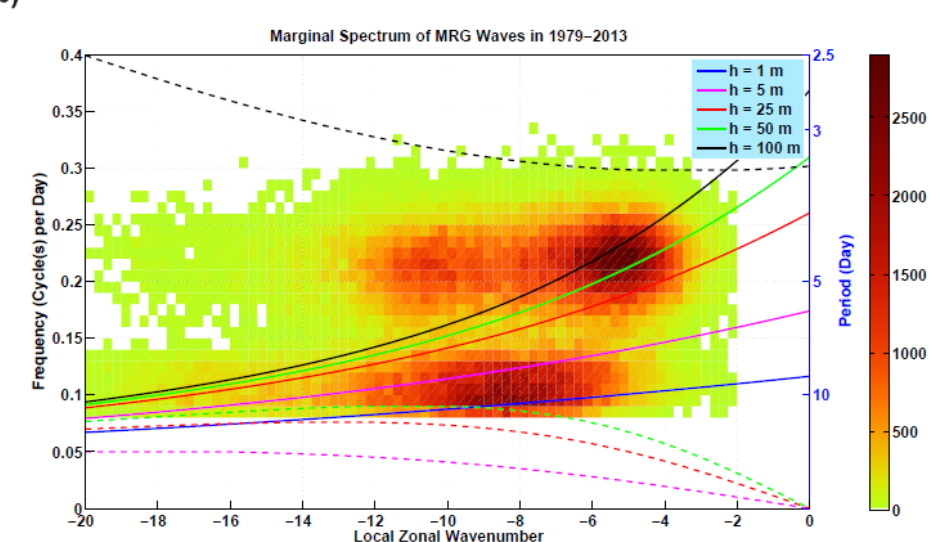


FIG. 10 Marginal zonal wavenumber-frequency spectra of global MRG waves from MEEMD components 3 and 4. a) MRG wave spectrum for year 2002; and b) MRG wave spectrum for years 1979-2013. The color scheme represents the summed energy projected onto the small bin of the zonal wavenumber-frequency domain. The solid curves are theoretical MRG wave dispersion relationship for equivalent depths (blue 1 m; pink 5m; red 25m; green 50m; and black 100 m). The dashed black curve is the theoretical dispersion relationship for n = 1 inertio-gravity wave with equivalent depth 5m. The green, red and pink dashed curves are theoretical n = 1 equatorial Rossby wave dispersion relationship for different equivalent depths (pink 5m; red 25m; and green 50m)

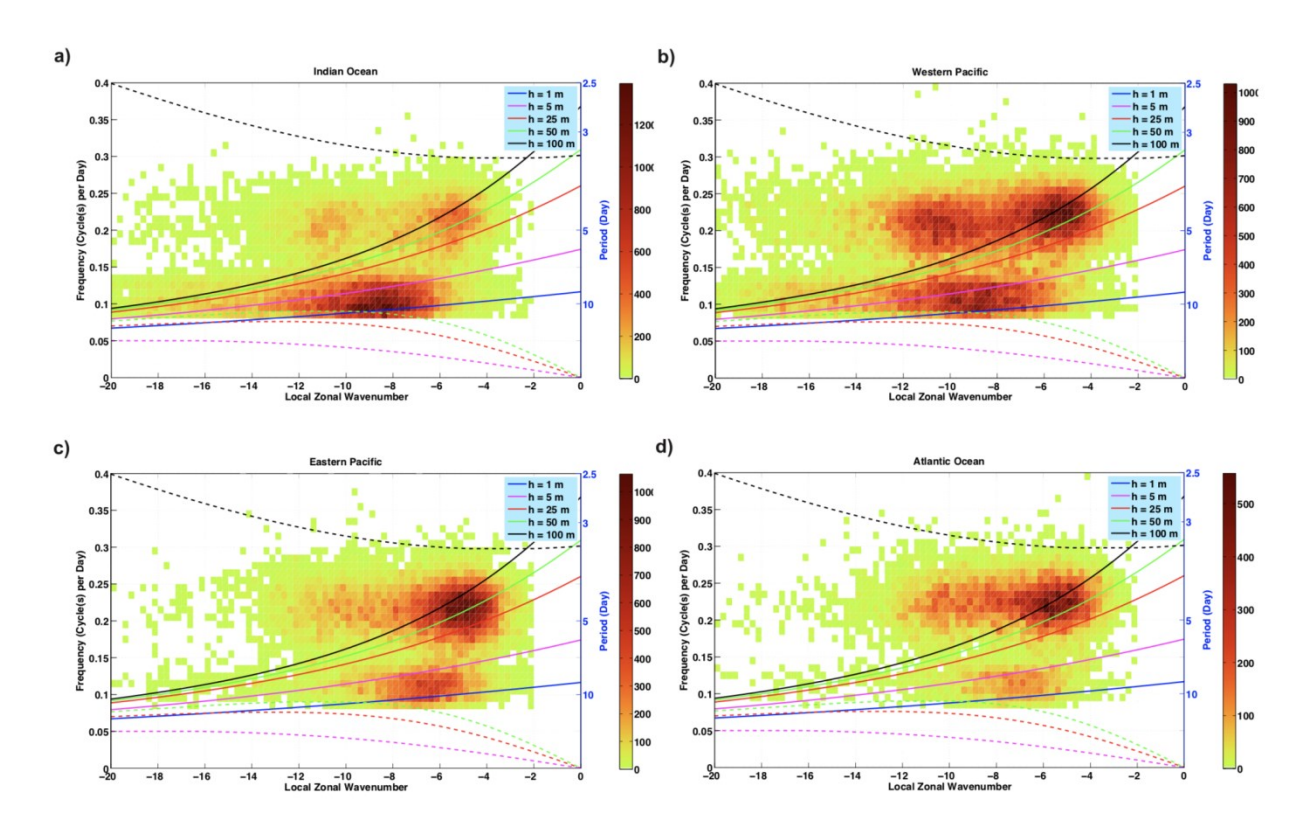


FIG. 11 The same as Fig.10b but for different regions for the period 1979-2013: a) Indian Ocean, b) western Pacific, c) eastern Pacific, and d) Atlantic Ocean

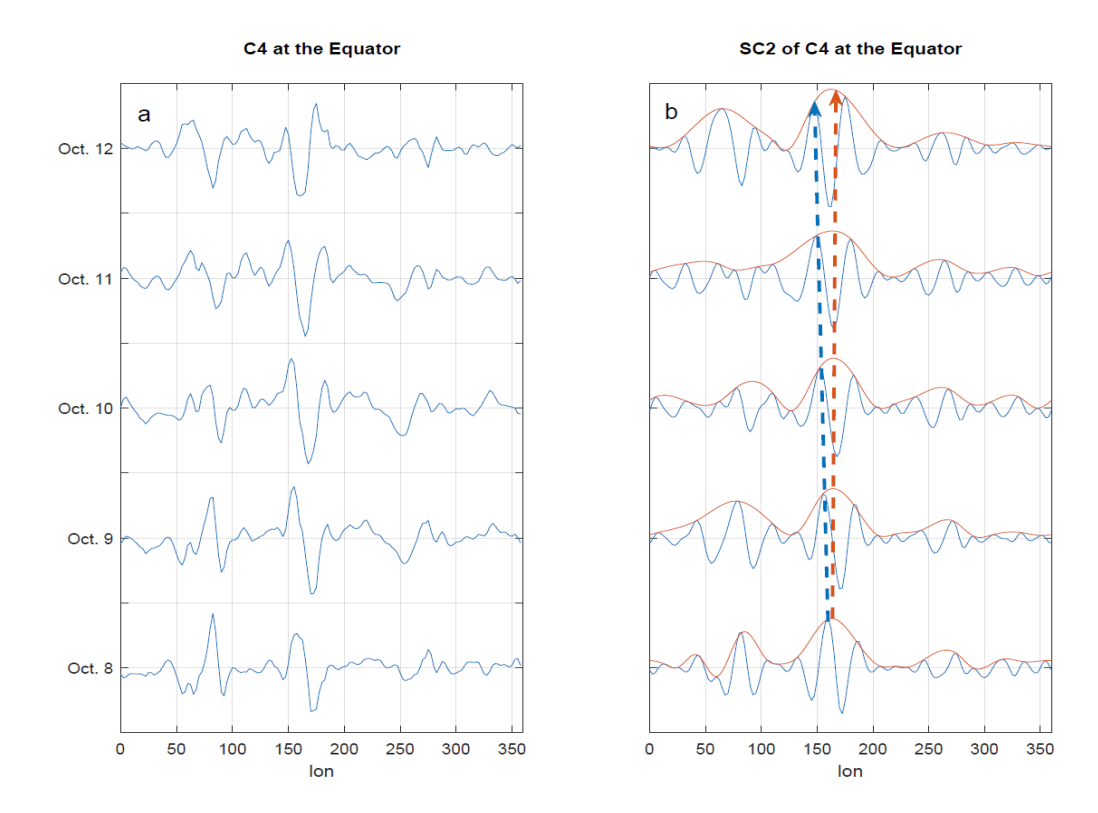


FIG. A1 The phase speed and group velocity of an MRG wave event. a) the sequential meridional winds along Equator from MEEMD component 4 for Oct. 8 to 12 of 2002, and b) their corresponding EEMD component 2's. The red curves are the envelops of EEMD components 2's. The blue dashed line indicates the phase speed and the red dashed line the group velocity

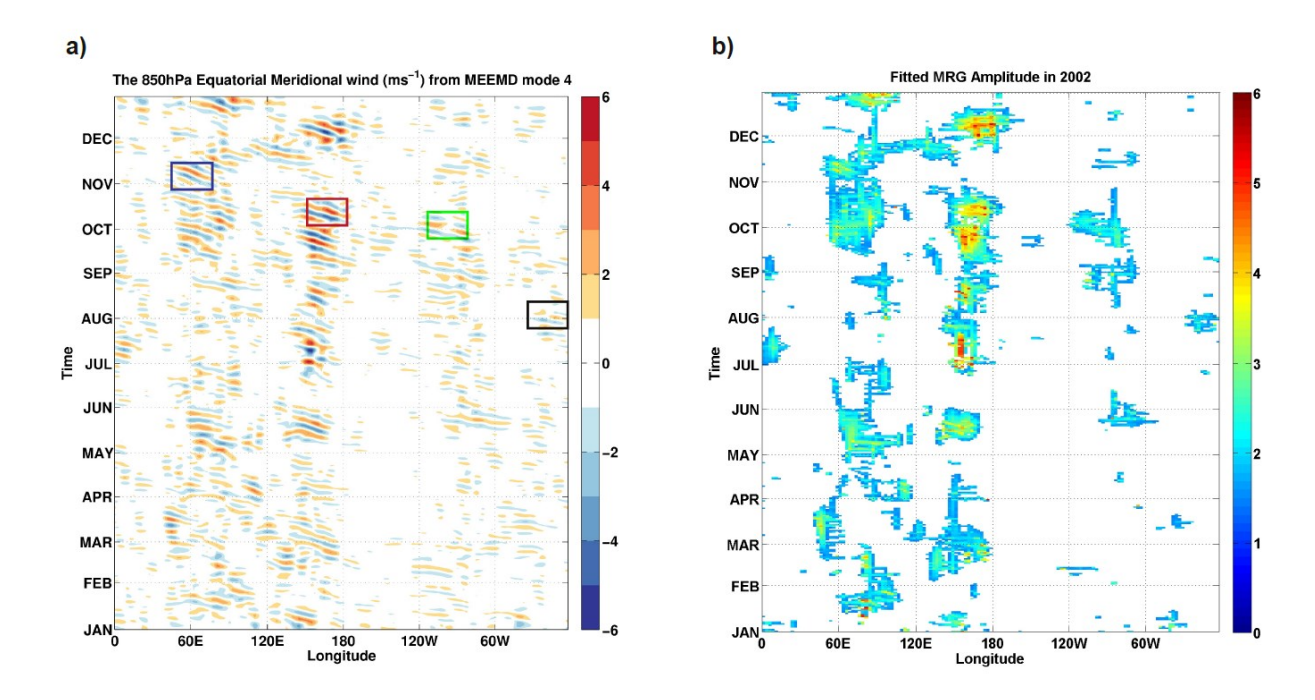


FIG. A2 The MEEMD 4th component of the meridional wind at the Equator (the same as Fig. 6) and the fitted amplitude. The values are indicated by the corresponding colorbars with a unit of ms⁻¹. In the right panel, regions with amplitude less than 1.5 ms⁻¹ is left blank